

RESEARCH ARTICLE

10.1002/2015JC011377

Turbulent flow field and air entrainment in laboratory plunging breaking waves

Byoungjoon Na¹, Kuang-An Chang¹, Zhi-Cheng Huang², and Ho-Joon Lim¹

Key Points:

- Estimating the size of energetic eddies and bubble size distribution
- Investigating the relation among bubble size distribution, void fraction, and turbulence
- Significantly higher turbulent dissipation rates occur when considering void fraction

Correspondence to:

K.-A. Chang,
kchang@tamu.edu

Citation:

Na, B., K.-A. Chang, Z.-C. Huang, and H.-J. Lim (2016), Turbulent flow field and air entrainment in laboratory plunging breaking waves, *J. Geophys. Res. Oceans*, 121, doi:10.1002/2015JC011377.

Received 6 OCT 2015

Accepted 4 APR 2016

Accepted article online 6 APR 2016

¹Zachry Department of Civil Engineering, Texas A&M University, College Station, Texas, USA, ²Graduate Institute of Hydrological and Oceanic Sciences, National Central University, Jhongli, Taoyuan, Taiwan

Abstract This paper presents laboratory measurements of turbulent flow fields and void fraction in deep-water plunging breaking waves using imaging and optical fiber techniques. Bubble-size distributions are also determined based on combined measurements of velocity and bubble residence time. The most excited mode of the local intermittency measure of the turbulent flow and its corresponding length scale are obtained using a wavelet-based method and found to correlate with the swirling strength and vorticity. Concentrated vortical structures with high intermittency are observed near the lower boundaries of the aerated rollers where the velocity shear is high; the length scale of the deduced eddies ranges from 0.05 to 0.15 times the wave height. The number of bubbles with a chord length less than 2 mm demonstrates good correlation with the swirling strength. The power-law scaling and the Hinze scale of the bubbles determined from the bubble chord length distribution compare favorably with existing measurements. The turbulent dissipation rate, accounting for void fraction, is estimated using mixture theory. When void fraction is not considered, the turbulent dissipation rate is underestimated by more than 70% in the initial impinging and the first splash-up roller. A significant discrepancy of approximately 67% between the total energy dissipation rate and the turbulence dissipation rate is found. Of this uncounted dissipation, 23% is caused by bubble-induced dissipation.

1. Introduction

Due to their highly turbulent and multiphase nature, investigating the physics, kinematics, and dynamics of breaking waves has been a challenging task to researchers for several decades. It has received attention due to its role in air-sea interactions and climate change [Melville *et al.*, 2002]. In the plunging breaking process, a two-phase flow region forms followed by air entrainment, which occurs immediately after an overturning jet impinges onto the undisturbed frontal water surface (and then this entrainment evolves over space and time). The air entrainment has been known to develop in several stages: the entrapment of air (i.e., an air cavity) caused by the plunging jet impinging the undisturbed water surface, air entrainment around the jet impinging point, additional air entrainment near the air water interface caused by subsequent splash-ups, air entrainment between the backside of the splash-up roller and the impinging roller, and entrainment all over the splash-up region in the later breaking stages [Kiger and Duncan, 2012]. A few measurement techniques have been developed to quantify bubble sizes and populations using a conductivity probe [Chanson, 2002; Mori *et al.*, 2007], an optical fiber probe [Lim *et al.*, 2008], and imaging and acoustics-based methods [Deane and Stokes, 2002]. However, few measurements on the formation and evolution of bubbles under breaking waves have been reported due to the insufficient temporal and spatial resolution of existing methods [Deane and Stokes, 2002]. Moreover, the effect of bubbles on the surrounding turbulence is still an enigma because of difficulties in conducting simultaneous measurements of void fraction and velocity in the presence of active air entrainment.

Studies of turbulent flow fields in breaking waves have shown great progress over the last two decades with advanced measurement techniques. Rapp and Melville [1990] applied flow visualization with a dye to observe turbulent mixing under unsteady laboratory-based breaking waves. They found that the penetration depth of the bubble cloud grows linearly over one to two wave periods, and then follows a power law of $t^{1/4}$ (with t being time). The bubble cloud evolves and reaches a depth of two to three wave heights and a horizontal length of one wavelength. Drazen and Melville [2009] used particle image velocimetry (PIV) to

measure the large-scale turbulent structure in post breaking velocity fields. The penetration depth (i.e., the vertical turbulent mixing length) was observed to follow an $x^{1/2}$ dependence, with x being the streamwise direction. The integral length scale of the energetic eddies was found to increase over time as the post breaking process continued. *Huang et al.* [2010] measured turbulent flow fields of surf-zone spilling breaking waves using PIV. They reported that the length scale of vortical structures was about 0.1–0.2 times the local water depth, and that the structures stretched downward as the waves propagated. The higher values of the local intermittency measure (*LIM*)—calculated through a wavelet transform—also spread downward, indicating that the vortical structures may significantly contribute to turbulence.

Coherent structures have been shown to be an important feature in turbulent flows, as they affect small-scale turbulence [*Bonnet and Delville*, 2001; *Camussi*, 2002]. Wavelet analysis has been shown to be a satisfactory tool to study the multiple scales of coherent structures [e.g., *Camussi and Felice*, 2006; *Longo*, 2009; *Ruppert-Felsot et al.*, 2009; *Huang et al.*, 2010]. *Camussi and Felice* [2006] used wavelet analysis to extract coherent structures in turbulent boundary layers. Their results showed that the mean size of coherent structures is about 4%–5% of the boundary layer thickness. *Longo* [2009] applied wavelet analysis to reduce the length scale of energetic eddies in the prebreaking region of surf-zone spilling breaking waves. He reported that the sizes of eddies that carry the most turbulence energy range from 10 times the Kolmogorov microscale to one wavelength. Similarly, *Huang et al.* [2010] revealed the existence of intermittent vortical structures under small-scale spilling breaking waves. It is, however, not clear how these swirling eddies would behave under the high foamy rollers and bubble clouds of plunging breaking waves.

Void fraction in the aerated region of breaking waves may affect the determination of certain physical quantities that involve fluid density. Without accounting for the void fraction, the kinetic energy, and potential energy could be overestimated by approximately 50% and 40%, respectively, during the breaking process of a plunging breaker [*Lim et al.*, 2015]. Measurement of void fraction in breaking waves has been progressing in both field and laboratory settings using acoustic, electrical, and optical methods [e.g., *Lamarre and Melville*, 1991, 1992; *Vagle and Farmer*, 1998; *Deane and Stokes*, 2002; *Chang et al.*, 2003; *Cox and Shin*, 2003; *Blenkinsopp and Chaplin*, 2007; *Rojas and Loewen*, 2007; *Lim et al.*, 2008; *Ryu and Chang*, 2008; *Lim et al.*, 2015]. However, only a small number of studies focused on the relation between void fraction and surrounding turbulent flows have been performed [e.g., *Cox and Shin*, 2003; *Mori and Kakuno*, 2008]. *Cox and Shin* [2003] used laser-Doppler velocimetry (LDV) and an impedance void fraction probe to measure the instantaneous velocity and void fraction above the trough level in the aerated region of surf-zone breaking waves. Their results showed that turbulent intensity and void fraction are positively correlated, following a linear relationship. *Mori and Kakuno* [2008] used a dual-tip resistance-type probe and acoustic Doppler velocimetry (ADV) to measure void fraction and flow velocities, respectively. They also found that the void fraction linearly correlates with the turbulence intensity. More recently, *Lim et al.* [2015] found a strong correlation among vorticity, turbulent intensity, and void fraction in the relatively lower void fraction region (void fraction between 0 and 0.6) at the initial impinging and the splashing stage of a deep-water plunging breaker.

Despite the advances made in these recent void fraction and turbulence studies, the relation between bubbles and turbulence in breaking waves has not been as well understood—especially in waves with high air entrainment and a large number of bubbles. *Baldy* [1993] reported that the bubble population distribution follows a power-law scaling value of -2 in wind generated breaking waves. *Garrett et al.* [2000] proposed that the bubble-size spectrum is proportional to a power-law scaling of $-10/3$ and that the rate at which larger bubbles fragment into smaller bubbles depends on the turbulent dissipation rate. They further modified the $-10/3$ power scaling and argued that the bubble-size spectrum became flatter at smaller scales (or steeper at larger scales) under the influence of dissolution and buoyancy forces. *Deane and Stokes* [2002] employed photographic, optical, and acoustical methods to measure void fraction and bubble-size distributions in both laboratory and open-ocean plunging breakers. They suggested that air entrainment in plunging breaking waves occurs due to two main mechanisms: smaller bubbles are formed by the impact, and subsequent splashing, of the overturning jet; while larger bubbles are formed by the fragmentation of the air “tube” or “vortex” trapped between the overturning jet and the wave face as the wave breaks. They showed two distinct power-law scaling relationships in bubble-size distributions: for bubbles with a diameter larger than about 1 mm, the bubble density spectrum was proportional to the bubble radius to the power of $-10/3$, while for smaller bubbles the spectrum showed a flatter -1.5 power-law scaling. *Mori*

et al. [2007] simultaneously measured flow velocities and bubble size distributions for breaking waves on a plane slope. They found a power-law scaling of -1.5 to -1.7 , independent of the experimental scale. The relationship among void fraction, turbulent intensity, and kinetic energy showed a linear dependence.

Recently, numerical simulations for the aerated wave-breaking flow were performed and validated with results from earlier laboratory experiments. *Shi et al.* [2010] proposed a two-fluid numerical model to simulate the evolution of air bubble plumes induced by deep-water breaking waves. Bubbles with a radius greater than O (1 mm) were found to have a major contribution on the void fraction, while smaller bubbles contribute significantly to the cross-sectional area of the bubble cloud (but not to the total volume of air). A strong, degassing effect on larger bubbles was found, caused by the fast decay of air patches consisting of higher void fraction (compared with those with lower void fraction). *Ma et al.* [2011] developed a polydisperse two-fluid model to simulate bubbly flows under surf zone breaking waves. The bubble-size spectrum was captured at different depths by the proposed model. They showed that, as the depth increases, the spectrum became steeper because of buoyancy. The simulated turbulent dissipation rate was also found to be much higher with the presence of bubbles. The bubble-induced turbulence suppression was linearly correlated with the void fraction in the high turbulence region. More recently, *Derakhti and Kirby* [2014] performed large-eddy simulations of a single breaking event in deep water. They found that bubble-induced dissipation accounts for more than 50% of the total dissipation. Their results also showed that the turbulent kinetic energy is damped by 20% by the dispersed bubbles in the plunging breaking wave. The numerical simulations were validated to a satisfactory degree with experiments, but a lack of simultaneous measurements of velocity and void fraction in the aerated region still contributes certain uncertainties, if not difficulties, in model validations.

The present study performed a laboratory experiment to quantify the highly aerated flow and bubbles under mechanically generated, unsteady plunging breaking waves in deep water. To measure velocities in the highly aerated region of breaking waves, a modified PIV technique and the bubble image velocimetry (BIV) technique were successfully used to obtain velocities inside and outside the aerated region [*Ryu et al.*, 2005; *Lim et al.*, 2015]. Moreover, void fraction in the aerated region was also measured using the fiber optic reflectometry (FOR) technique [*Chang et al.*, 2003; *Lim et al.*, 2008]. Using the measured velocity and corresponding residence time for each bubble encounter, bubble chord lengths were obtained at three vertical cross sections. The present study is an extension of *Lim et al.* [2015], with a special focus on the relation between turbulence flow fields and bubbles generated by wave breaking. In section 2, the wave generation and experimental setup is described. In section 3, the distribution of local maximum of the local intermittency measure is presented using a wavelet-based technique. The local energy content is then compared with the vorticity and swirling strength. Subsequently, the length scales of vortical structures are estimated. In section 4, void fraction and bubble chord length distributions are determined and their relation with turbulence properties is discussed. Correlations between void fraction, bubble-size distribution, and certain flow characteristics are also presented. Finally in section 5, turbulence dissipation rates—considering void fraction—are obtained based on the measurement data using a mixture theory of two-phase flows. The role of bubbles in the energy budget is also investigated.

2. Experimental Setup

The experiment was carried out in a two-dimensional wave tank located in the Department of Civil Engineering at Texas A&M University. The tank was 35 m long, 0.91 m wide, and 1.2 m deep, and is equipped with a flap-type wavemaker at one end. A 1:5.5 sloping beach with a layer of horsehair was located at the opposite end to absorb wave energy and reduce reflection. A constant water depth of $h = 0.80$ m was maintained throughout the experiment.

A plunging breaking wave was generated using a wave focusing technique similar to *Skyner* [1996]. The wave packet consists of 13 waves of various wave numbers and amplitudes with a central frequency of $f_c = 1.1$ Hz. Only one plunging breaking wave that broke at the desired location, with good repeatability, was generated in each run. The primary breaking wave has a wave height of $H = 0.204$ m and a wave period of $T = 0.83$ s. Based on linear wave theory, the wavelength is $L = 1.08$ m, the phase speed is $C = 1.30$ m/s, the wave steepness H/L is 0.19, and the wave is in a deep water condition of $kh = 4.7$ (with k being the wave number). The coordinate system is defined such that x represents the horizontal direction (along the

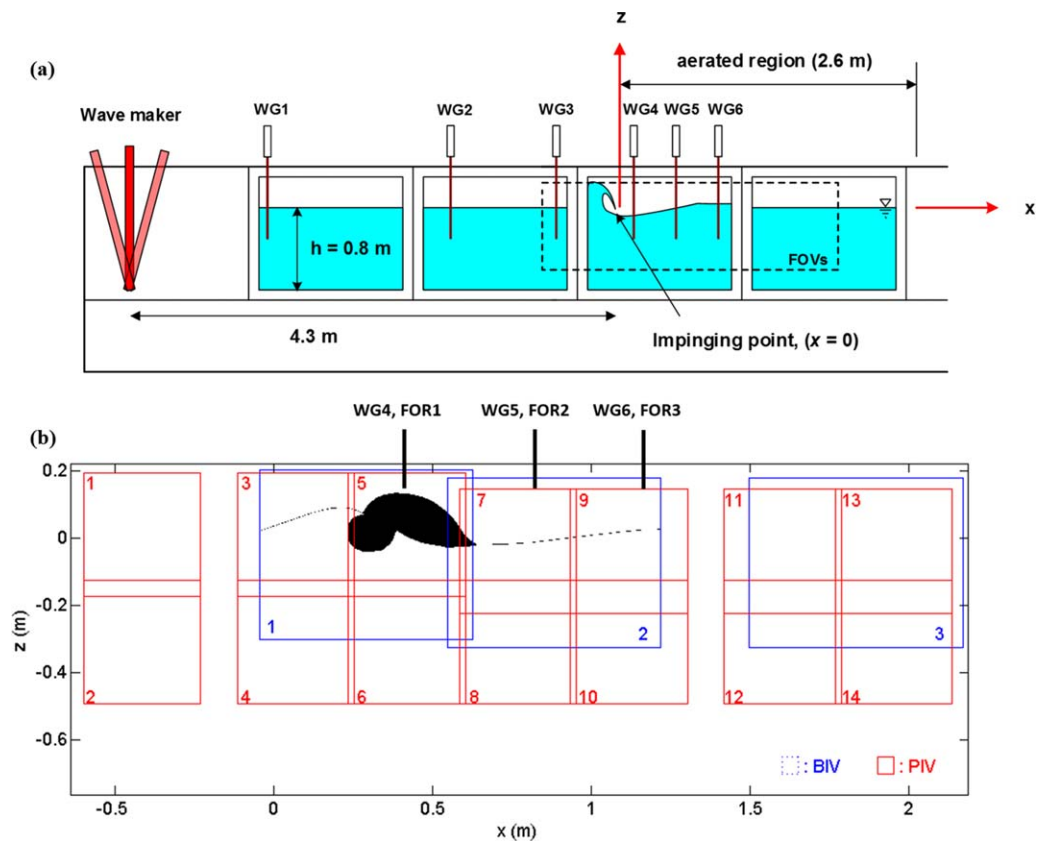


Figure 1. (a) Sketch of the wave tank and locations of the wave gauges. (b) Detailed locations of the PIV and BIV fields of view with the aerated region masked as black (at $t = 0.25$ s).

wave propagation), y the cross tank direction, and z the vertical upward direction. The origin $x=0$ and $z = 0$ is defined as the impinging point of the breaking wave and the still water level, and time $t = 0$ is defined as the moment of wave impingement. More details of the experiment can be found in *Lim et al.* [2015].

A brief description of the measurement methods employed in the study is provided below, and more details can be found in *Lim et al.* [2015]. In the experiment, wave gauges, along with BIV, modified PIV, and FOR techniques were used to measure surface elevation, flow velocities, and void fraction of breaking waves. The BIV technique measures the velocity field of the aerated region in the breaking waves and the free surface. The modified PIV technique measures the entire flow field, including the prebreaking region and the highly aerated region. The FOR technique detects phase changes and obtains the bubble residence time (and therefore the void fraction) at three vertical stations located at the three splash-up regions coincident with the three wave gauge locations. A total of 20 repeated runs were performed with the same test conditions at each measurement location for all the measurements. The measured data obtained include 14 field of views (FOVs) in the PIV measurements with 20 repeated runs for each FOV (a total of 280 runs), 3 FOVs in the BIV measurements with 20 repeated runs each (a total of 60 runs), 38 FOR measurement points with 20 repeated runs each (a total of 760 runs), and 6 wave gauge measurements with 20 repeated runs (a total of 20 runs). The mean and fluctuating quantities were calculated from ensemble averaging the 20 instantaneous measurements. *Lim et al.* [2015] showed that the averaged root-mean-square values of the measured free surface data before breaking range from 0.32% to 0.35% of the primary breaking wave height H , indicating high repeatability of the generated waves. They also estimated the measurement uncertainties on velocity and void fraction and concluded that the estimated errors are 4.6% and 0.17 at most, respectively.

The free surface profiles were measured using six double-wired resistance-type wave gauges (termed WG1 to WG6) at $x = -2.98, -1.31, -0.57, 0.43, 0.88,$ and 1.20 m as shown in Figures 1a and 1b. The location of WG3 was set a short distance (0.17 m) upstream from where the front face of the plunging breaker

becomes vertical. WG4, WG5, and WG6 were set in the middle of the first three splash-up regions where the splash-ups were fully developed. These three wave gauges are coincident with the three FOV measurement stations (termed FOV1–FOV3).

The BIV technique [Ryu *et al.*, 2005] was used to measure the velocity field in the aerated region after the primary breaking wave impinges onto its front surface. The images were captured by a high speed camera that has a resolution of 1024×1024 pixels and a 10 bit dynamic range. The framing rate was set at 500 frames per second throughout the experiment. Two regular 600 W light bulbs with reflecting mounts and a translucent flat plate were used to illuminate the flow from behind the tank. The depth of field for the captured images is 0.21 m with its center at 0.2 m behind the tank's front wall. Three FOVs of 0.66×0.50 m² were used to cover the entire aerated region of the plunging breaker as shown in Figure 1b. There was a small overlap region of 84 mm between FOV1 and FOV2, and a gap of 270 mm between FOV2 and FOV3 due to a steel column supporting the wave tank. After acquiring the images, velocities were determined using commercial software from LaVision Inc. An adaptive multipass algorithm—which has an initial interrogation window of 32×32 pixels and a final window of 16×16 pixels, with a 50% overlap—was applied in the process. Accordingly, the final resolution of the velocity vectors was 8×8 pixels, corresponding to 5.26×5.26 mm². The BIV images were also used to obtain the free surface information and to identify the aerated region. Both the principle and the validation of the BIV technique are detailed in Ryu *et al.* [2005], Ryu and Chang [2008], and Lin *et al.* [2012].

The modified PIV technique was used to measure the velocity fields in the entire breaking region using a weak, continuous laser and a high dynamic range camera with a short exposure time [Lim *et al.*, 2015]. A 5 W continuous Argon-Ion laser was used as the light source, and two cylindrical concave lenses were used to generate the wide light sheet. The same camera and framing rate as in the BIV measurements were used in the PIV measurements. In the PIV measurements, 14 FOVs centered at 0.2 m behind the tank's front wall were used to cover the entire flow field of breaking waves. The sizes of the 14 FOVs (see Figure 1b) were fixed as 0.37×0.37 m². Similar to the image processing in BIV, the velocity maps were obtained using the adaptive multipass algorithm with an initial interrogation window of 64×64 pixels and a final window of 32×32 pixels, with a 50% overlap. The resolution of the velocity vectors is 16×16 pixels, corresponding to 5.78×5.78 mm². There is an overlap of 20 mm between adjacent FOVs. Using the mosaic concept, the 14 FOVs cover the entire flow field of the plunging breaker with sufficient spatial and temporal resolutions.

The FOR technique was used to obtain the bubble residence time and the void fraction in the aerated region of the breaking wave. FOR is capable of distinguishing air and water based on the coherent mixing of scattered signals with the Fresnel reflection from the tip of an optical fiber. FOR is a point measurement tool, and is nearly noninvasive due to the small diameter of the fiber (~ 125 μ m). More details on the principle, validation, and applications of FOR can be found in Chang *et al.* [2002, 2003], Lim *et al.* [2008], Ryu and Chang [2008], and Lim *et al.* [2015]. The sampling rate of the FOR measurements was set at 100 kHz throughout the experiment. The measurements were taken at three FOR measurement stations located at the middle of the three splash-ups of the breaking wave. The total number of measurement points at FOR stations 1, 2, and 3 were 19, 12, and 7, respectively, with a constant interval of 10 mm. These numbers were determined by the vertical spreading of the bubble cloud at each station.

3. Evolution of Turbulent Flow Fields

3.1. Extracting Vortical Structures Using Wavelet Analysis

During the formation of the plunging breaking wave, the overturning water jet falls and impacts on the water surface ahead of it, generating the first impinging roller. This impact produces a large upward momentum, leading to the first splash-up roller. Figure 2 shows a sample of the instantaneous velocities measured by PIV on a moving frame of the phase speed, C , for easy identification of the rollers. Evidently, the first impinging roller and the first splash-up roller are visible in Figures 2c and 2d. More details about the breaking process of the plunging breaker have been presented in Lim *et al.* [2015], so they are not repeated here.

Identifying vortex-like coherent structures is essential in studying the dynamics of turbulent flows. In the present study, vortical structures under the deep water breaking waves were deduced using a wavelet transform with a Morlet wavelet $\varphi(z)$ defined as follows:

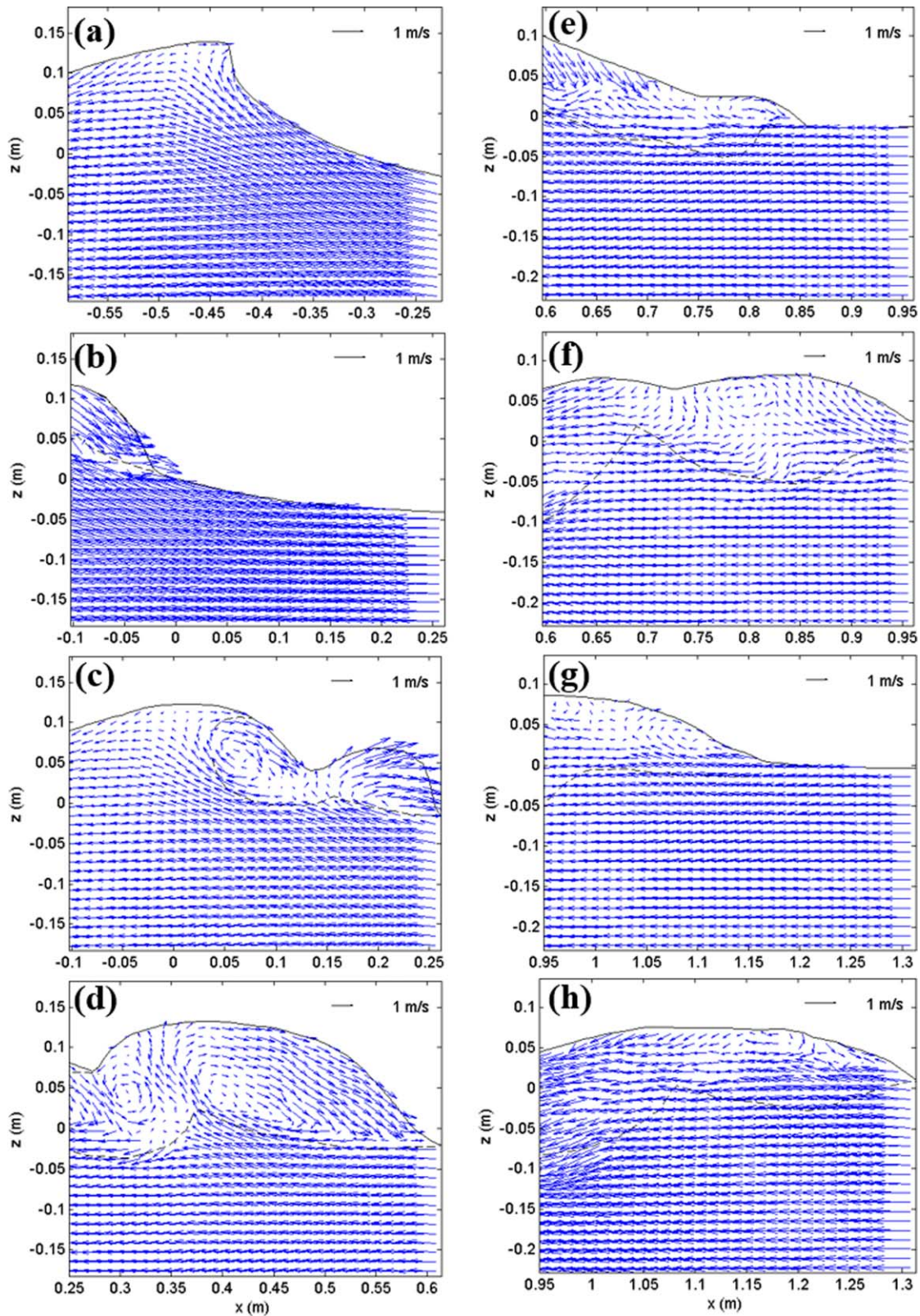


Figure 2. Sample instantaneous velocity fields on a moving frame of the phase speed, C , during the breaking process: (a) $t = -0.2$ s (FOV1, prebreaking), (b) $t = -0.02$ s (FOV3), (c) $t = 0.09$ s (FOV3, beginning of the first splash-up), (d) $t = 0.25$ s (FOV5, fully developed first splash-up), (e) $t = 0.41$ s (FOV7, beginning of the second splash-up), (f) $t = 0.56$ s (FOV7, fully developed second splash-up), (g) $t = 0.68$ s (FOV9, beginning of the third splash-up), and (h) $t = 0.80$ s (FOV9, fully developed third splash-up). Only one quarter (in every other row and every other column) of the measured velocity vectors are plotted. The dashed lines represent the boundary of the aerated region determined using the BIV images.

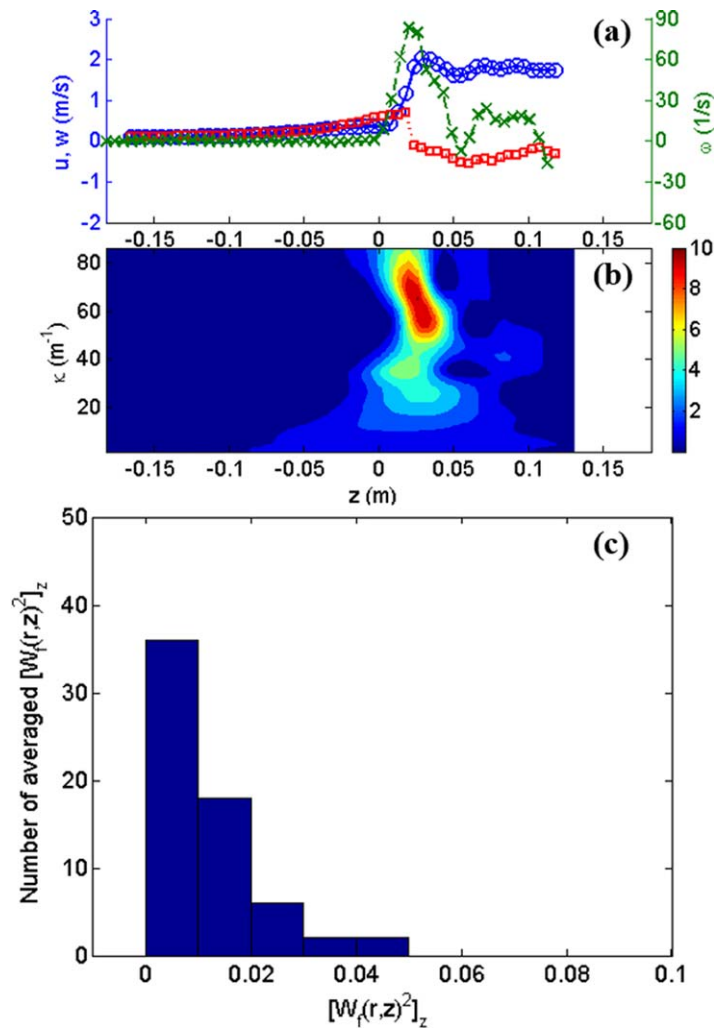


Figure 3. (a) Sample vertical distributions of velocities at $x = 0.41$ m in FOV5 (fully developed first splash-up with a time instant corresponding to Figure 2d). In the plot, u (circle), w (square), and ω (cross) denote the streamwise velocity, vertical velocity, and vorticity, respectively. (b) Corresponding contour map of LIM against wave number κ and vertical location z . (c) Histogram of $\langle [w(s, z)]^2 \rangle_z$.

the flow into dynamically coherent vortices and incoherent background flow. A quantitative local intermittency measure (LIM) introduced by Farge [1992] is defined as follows:

$$LIM(s, z) = \frac{[W_f(s, z)]^2}{\langle [W_f(s, z)]^2 \rangle_z} \quad (3)$$

where $\langle [W_f(s, z)]^2 \rangle_z$ is the average of the square of a wavelet coefficient along the z direction. LIM has been successfully adopted in analyzing turbulent flows for eddy detection [e.g., Camussi, 2002; Camussi and Felice, 2006; Longo, 2009]. In the present study, this method is modified to make it applicable to flows that feature both turbulent and laminar regions—such as the combined aerated turbulent region, and the unaerated laminar region below and behind it, in the present deep-water breaking waves. The inherent normalization process would otherwise contaminate the values of LIM in the region where most wavelet coefficients are small (e.g., the laminar flow region behind and below the highly turbulent impinging roller).

Figure 3a shows sample instantaneous velocities (u , w) and vorticity (ω), and Figure 3b shows the corresponding LIM at a vertical column located approximately in the middle of the fully developed first splash-up in FOV5. The figures indicate that the high LIM values coincide with the presence of vortical structures in

$$\varphi(z) = e^{iw_0 z} e^{-z^2/2} \quad (1)$$

where z is the position of the signal for the (different) window of the mother wavelet, and $w_0 = 6$ is suggested to satisfy the admissibility condition [Farge, 1992]. It has been verified that the physical results do not depend on the choice of the mother wavelet [Farge, 1992; Camussi and Felice, 2006]. The wavelet coefficient of a velocity signal is then defined as the following using the continuous wavelet transform [Farge, 1992]:

$$W_f(s, z) = \frac{1}{\sqrt{s}} \int_{-\infty}^{\infty} u(\tau) \varphi^* \left(\frac{\tau - z}{s} \right) d\tau \quad (2)$$

where $u(\tau)$ is the horizontal velocity, s is the scale dilation parameter, τ is the translation parameter, \sqrt{s} is for energy normalization across the different scales, $*$ denotes the complex conjugate, and the integrand represents a convolution product between the dilated and translated counterpart of the complex conjugate of the mother wavelet. In calculating the wavelet coefficients, the boundary values were extended and kept at the same values to minimize boundary effects.

Wavelet transform in signal analysis is capable of splitting

the turbulent flow region. *Camussi and Felice* [2006] showed that the location of a *LIM* peak matches the location of the corresponding coherent structure by comparing the *LIM* field and the vorticity field. Accordingly the corresponding turbulent length scale may be determined directly from the wavelet transform results.

The distribution of $\langle [W_f(s, z)]^2 \rangle_z$ is shown in Figure 3c as a histogram. It is worth pointing out that the level of *LIM* in the prebreaking region, such as the velocity field show in FOV1, was found comparable to that in the splash-up region. This is caused by the inherent normalization process (i.e., a small value normalized by another small value) in equation (3). The normalization process forces the *LIM* values in the laminar region to have a similar magnitude as those in the turbulent region, which in turn leads to the failure of the *LIM* approach in the laminar region. Nevertheless, it was found that the distribution of $\langle [W_f(s, z)]^2 \rangle_z$ in the turbulent flow region is distinct to that in the presumably laminar region. To counter the problem, setting a threshold value may be needed to distinguish the laminar and turbulent regions. It was found that the distributions are noticeably different in the vicinity of $\langle [W_f(s, z)]^2 \rangle_z = 0.01$. Therefore, velocity vectors in a water column with $\langle [W_f(s, z)]^2 \rangle_z$ less than 0.01 were identified as the laminar flow region, and a constant value of $LIM = 0.01$ was assigned to them. This conditional threshold is necessary to separate the laminar flow region where the *LIM* approach is not applicable.

3.2. Evolution of Vortical Structures

Camussi [2002] reported that the peak of *LIM* matches the vortex core, and that the location of the vortical structure can be identified by locating the *LIM* peak. The *LIM* peak among different scales can be formulated as

$$LIMM(z) = \max \{LIM(s, z)\} \quad (4)$$

The value of *LIMM* represents the energy level of the most excited mode among the scale bands. *Camussi and Felice* [2006] reported that inverting the scale dilation parameter of *LIMM* directly gives the length scale of the identified vortex. It has been previously suggested that a conditional threshold technique could be applied to remove the “background noise” induced by the mean shear caused by waves, so as to extract the vortical structures induced by turbulence [*Cox and Kobayashi*, 2000; *Huang et al.*, 2010]. *Cox and Kobayashi* found that the instantaneous turbulent kinetic energy and the instantaneous Reynolds stresses are several times greater than the phase-averaged background values. In the present study, high mean shear stresses were observed along the lower boundary of the aerated region due to the differential motion between the high-speed rotation in the first splash-up roller region and the relative low-speed wave motion under the trough level. Thus, the conditional threshold technique was applied to extract the turbulence-induced vortical structures.

Figure 4 shows the evolution of instantaneous *LIMM* fields with the conditional threshold technique being applied. A condensed region with high values of intermittency is observed within the aerated region. At the initial stages of wave breaking (Figures 4b and 4c), high values of *LIMM* were observed near the lower boundary of the aerated region, consistent with the distribution of turbulent intensity [*Lim et al.*, 2015]. As the wave propagates, the high values of *LIMM* spread across the aerated region at the later stages (Figures 4d–4f). Note that the level of *LIMM* remains high at the second splash-up roller (Figure 4f) and at the third splash-up roller (Figure 4h), as compared to that of the first splash-up roller (Figure 4d). This result is consistent with the similar level of turbulence maintained even at the weak third splash-up roller, as reported in *Lim et al.* [2015]. They also reported a very low void fraction observed at the third splash-up roller, but the passage of bubbles may contribute to the high level of turbulence in the later stages of breaking.

Figure 5 shows the distributions of the corresponding instantaneous length scales (*LS*) of the vortical structures. The length scales were directly calculated by inverting the wavenumber κ (i.e., the reciprocal of the scale dilation parameter) at which the *LIMM* was sought. The length scales in the highly aerated region are mostly lower than one half of the wave height of the breaking wave. In comparison, the length scales in surf-zone breakers were found to vary from between the breaker height and the wavelength in *Longo* [2009] to less than one half of the water depth in *Huang et al.* [2010].

3.3. Comparison of *LIMM*, *LS*, Swirling Strength, and Vorticity

The *LIMM* fields were compared and validated with the corresponding swirling strength and vorticity fields. Swirling strength can be computed based on the local velocity gradient tensor. It has been applied in 2-D

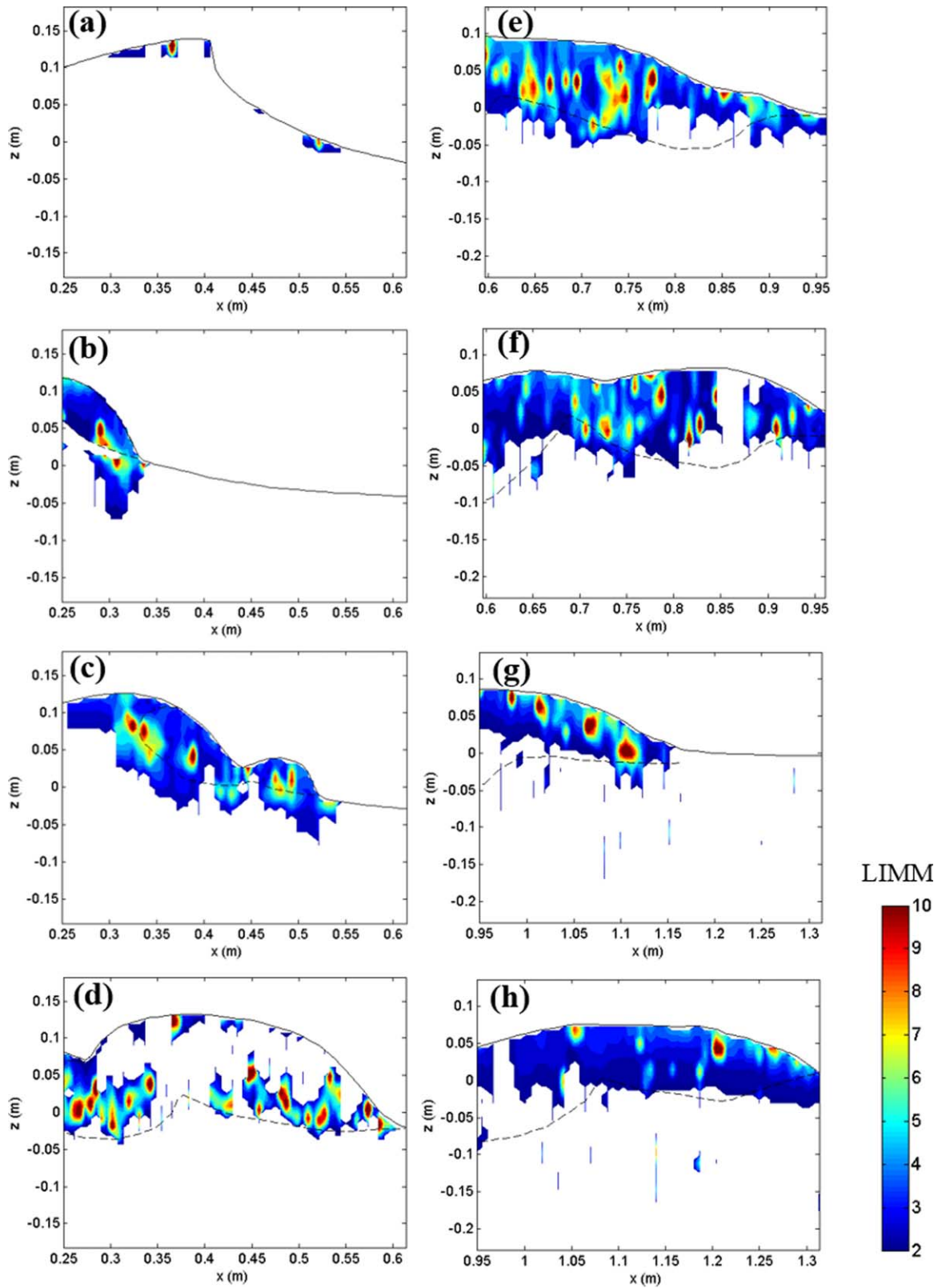


Figure 4. Instantaneous LIMM fields corresponding to Figure 2.

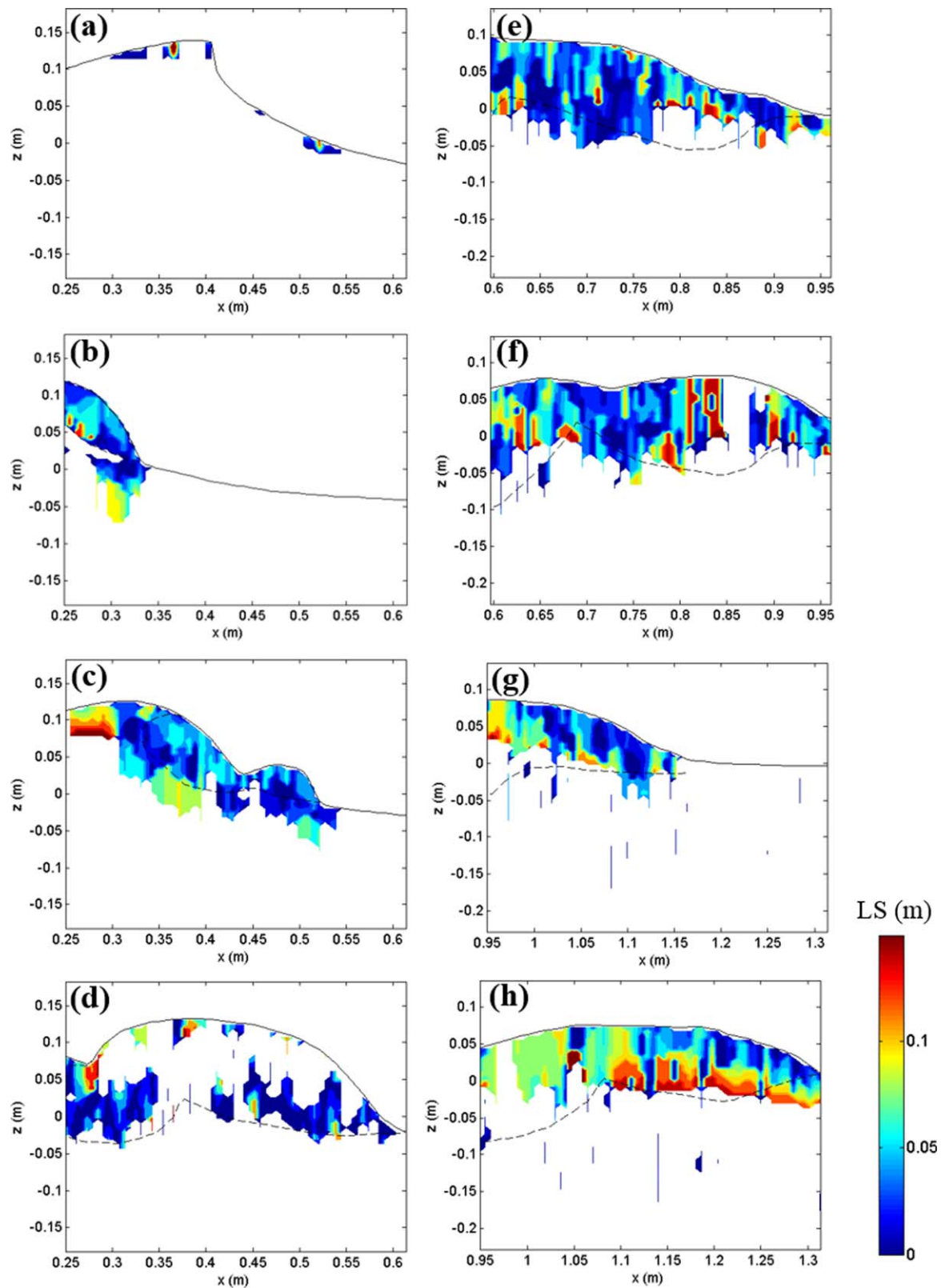


Figure 5. Instantaneous length scale (LS) fields corresponding to Figures 2 and 4.

as well as 3-D flow fields [Zhou et al., 1999; Adrian et al., 2000; Camussi, 2002]. The swirling strength, ψ , is defined as the imaginary eigenvalue of the local deformation matrix (DM) as follows:

$$DM = \begin{bmatrix} \frac{\partial u}{\partial x} & \frac{\partial u}{\partial z} \\ \frac{\partial w}{\partial x} & \frac{\partial w}{\partial z} \end{bmatrix} \quad (5)$$

Vorticity fields were also computed for the identification of vortical structures. Root-squared vorticity, $\omega^* = \sqrt{\omega^2}$, was used for the comparison because $LIMM$ is always positive (so we are unable to distinguish the rotation direction for a vortical structure). Central differences were used to compute the spatial velocity gradients. To be consistent with the dimensionless $LIMM$, swirling strength and root-squared vorticity were also nondimensionalized over its corresponding column averaged value as follows:

$$\Psi = \frac{\psi}{\langle \psi \rangle_z} \quad (6)$$

$$\Omega = \frac{\omega^*}{\langle \omega^* \rangle_z}$$

where $\langle \rangle_z$ denote the average along the z direction.

Figure 6 shows the evolution of the ensemble averaged $LIMM$, $1/LS$, Ψ , and Ω over the 20 measured instantaneous fields. Note that the spatial resolution corresponding to the wavelet analysis is one half the Nyquist wavenumber ($\sim 86.5 \text{ m}^{-1}$), corresponding to about 0.01 m in the present study. This implies that the size of the vortices needs to be greater than 0.01 m for a reliable comparison. Overall, good agreement was found among the four variables at most stages of the breaking process. At the earlier stages of breaking shown in Figures 6b–6d, the condensed region with high values of $LIMM$, $1/LS$, Ψ , and Ω is consistently observed at the lower boundary of the aerated region. The concentrated region, with high values of $LIMM$, is found close to the centers of the first splash-up and the first impinging rollers when the splash-up roller is fully developed. Despite the similar patterns among $LIMM$, $1/LS$, Ψ , and Ω , the evolution of $LIMM$ is more similar to that of turbulent intensity as reported in Lim et al. [2015]. This is consistent with the results showing that eddies carry most of their turbulence energy under the wave crest phase [Longo, 2003]. The condensed region elongates and spreads across the aerated region as turbulence continues to generate and diffuse at the later stages of breaking (Figures 6e–6h). For the condensed spots within the aerated rollers, those with higher values of $LIMM$ seem to be more widely spread in comparison to those with high Ψ and Ω . This is probably because eddies with different scales all contribute to the determination of $LIMM$, whereas only the local velocity gradients are used in calculating Ψ and Ω .

It is practical to calculate $LIMM$ using wavelet analysis to determine length scales of eddies. For example, the length scale of the eddies corresponding to the condensed high values of $LIMM$ at the center of the impinging roller marked by the left circle in the top left plot of Figure 6d is about 0.05 m ($1/LS = 20 \text{ m}^{-1}$), as shown in the left circle of the top right plot of Figure 6d. That length is roughly the size of the condensed region, which itself has high $LIMM$ values. On the other hand, the length scale of the eddies near the lower boundary of the splash-up roller ranges from 0.03 to 0.05 m, as shown in the right circle of the top right plot of Figure 6d, which implies that the region contains a number of smaller eddies. One may also infer from the good correlation between $1/LS$ and the swirling strength that these smaller eddies feature more intense swirling motions. The similar patterns among $LIMM$, $1/LS$, Ψ , and Ω indicate that the wavelet-based technique can be successfully applied to identify vortical structures and their length scales in deep water plunging breakers in the presence of an intense air entrainment.

Figure 7 shows the evolution of wave height normalized by ensemble-averaged length scales. In the region near the lower boundary of the aerated roller during the initial impinging and the first splash-up stages (Figures 7b and 7c), the value of H/LS ranges from about 7 to 20, which corresponds to the length scales of eddies from about $0.05H$ – $0.15H$ (or 1–3 cm). As the breaking wave propagates, the splash-up roller and the impinging roller both begin to stretch horizontally and their length scales increase. While the most energetic eddies are able to retain their length scales at close to H for about one wave period (Figures 7a–7e), the length scales eventually increase after that (i.e., after Figure 7f). The value of H/LS outside the aerated region is mostly less than 1.7 (i.e., the length scales outside the aerated region are mostly greater than $0.6H$).

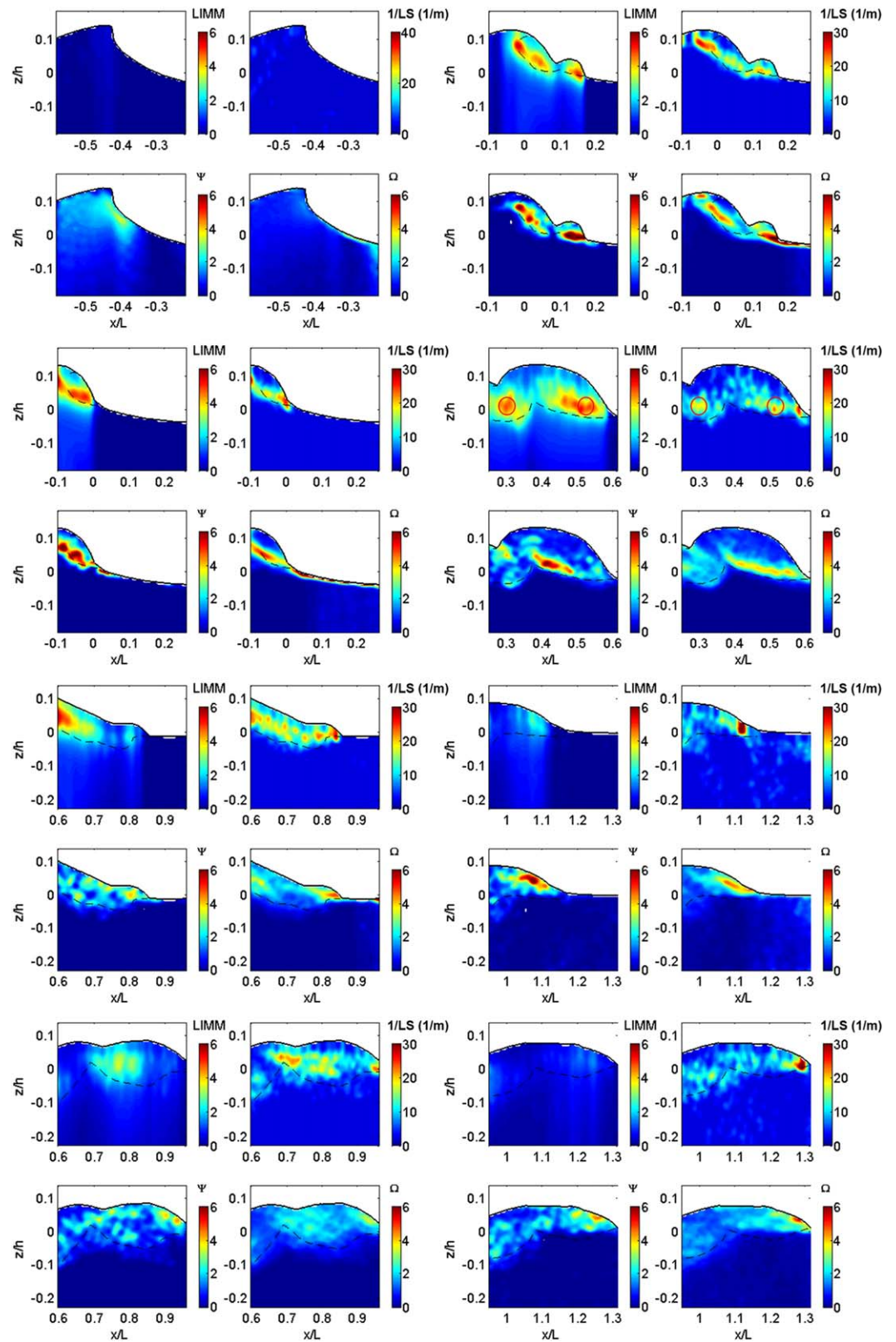


Figure 6. Evolution of ensemble averaged $LIMM$, $1/LS$ (m^{-1}), nondimensionalized swirling strength (Ψ), and nondimensionalized vorticity (Ω) corresponding to the instants and locations in Figure 2.

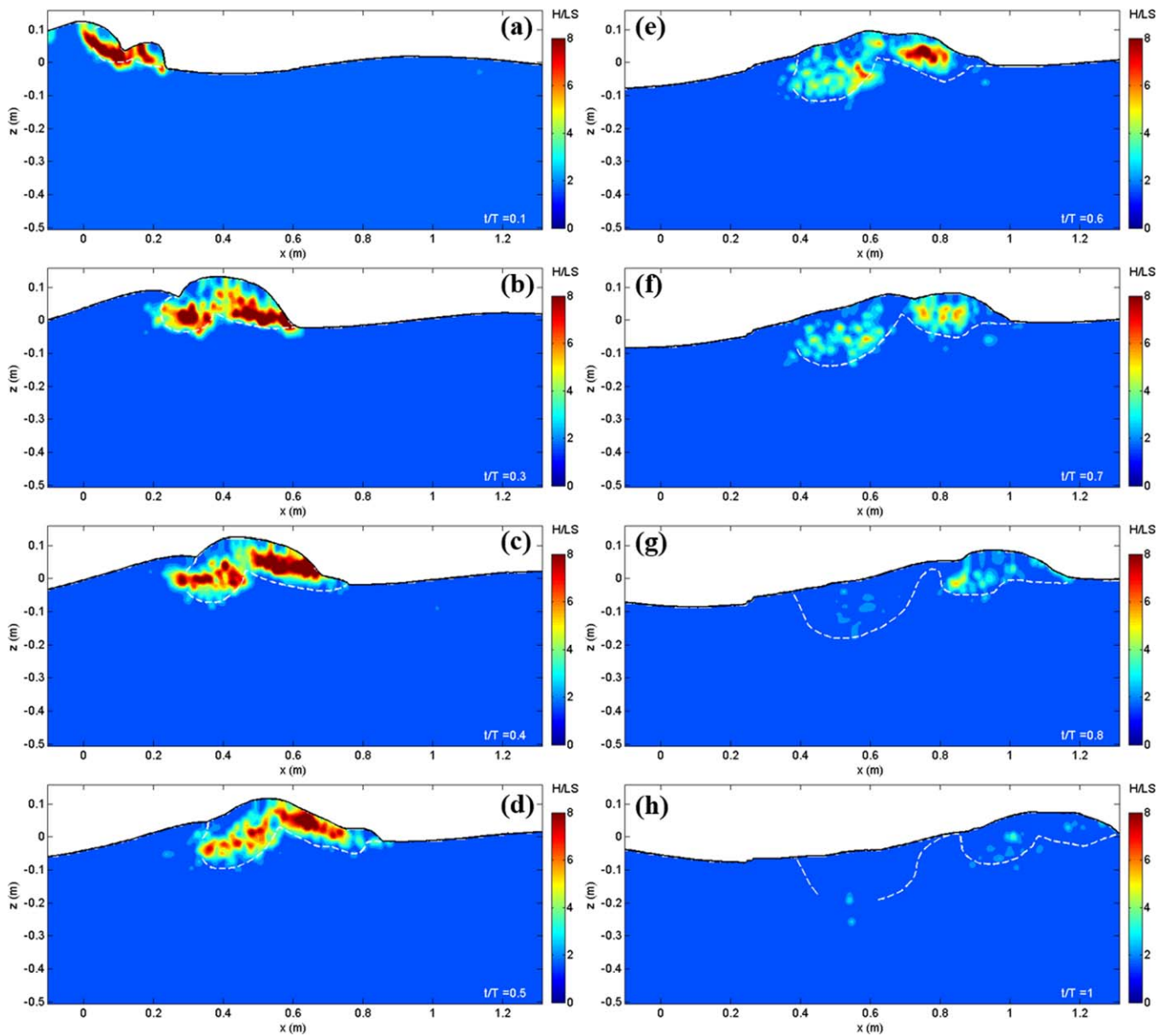


Figure 7. Evolution of the normalized length scale (H/LS) at $t/T =$ (a) 0.1, (b) 0.3, (c) 0.4 s, (d) 0.5, (e) 0.6, (f) 0.7, (g) 0.8, and (h) 1.0. The dashed lines are boundaries of the aerated region identified from the BIV images.

or 12 cm). Note that the *LIM* approach is not applicable to the presumably laminar region outside the aerated region, so a constant value of *LIM* was assigned in the present study. This implies that the approach applying *LIMM* fails to estimate a meaningful length scale outside the aerated region. *Govender et al.* [2004] found that eddies in the surf-zone spilling breakers show a general increase of length scale, from wave crest downward, ranging from about $0.1h$ to $0.4h$. With similar physical dimensions, their eddy length scale near the surface is around 2 cm—which is comparable to the physical dimensions of the eddy length scale of 1–3 cm in the aerated region in the present study. It suggests that the confining effect of the bed on eddy sizes in the breaking waves is likely insignificant. Moreover, *Huang et al.* [2010] showed that the length scale of eddies near the crest region in surf-zone breaking waves is close to—but about one half of—that in the present study.

The wavelet-resolved length scale inside the highly aerated region of the plunging breaking waves was compared with a classical turbulent length scale estimate based on autocorrelation. The integral length scale is a measure of the characteristic length of the energetic eddies in the flow. The integral time scale

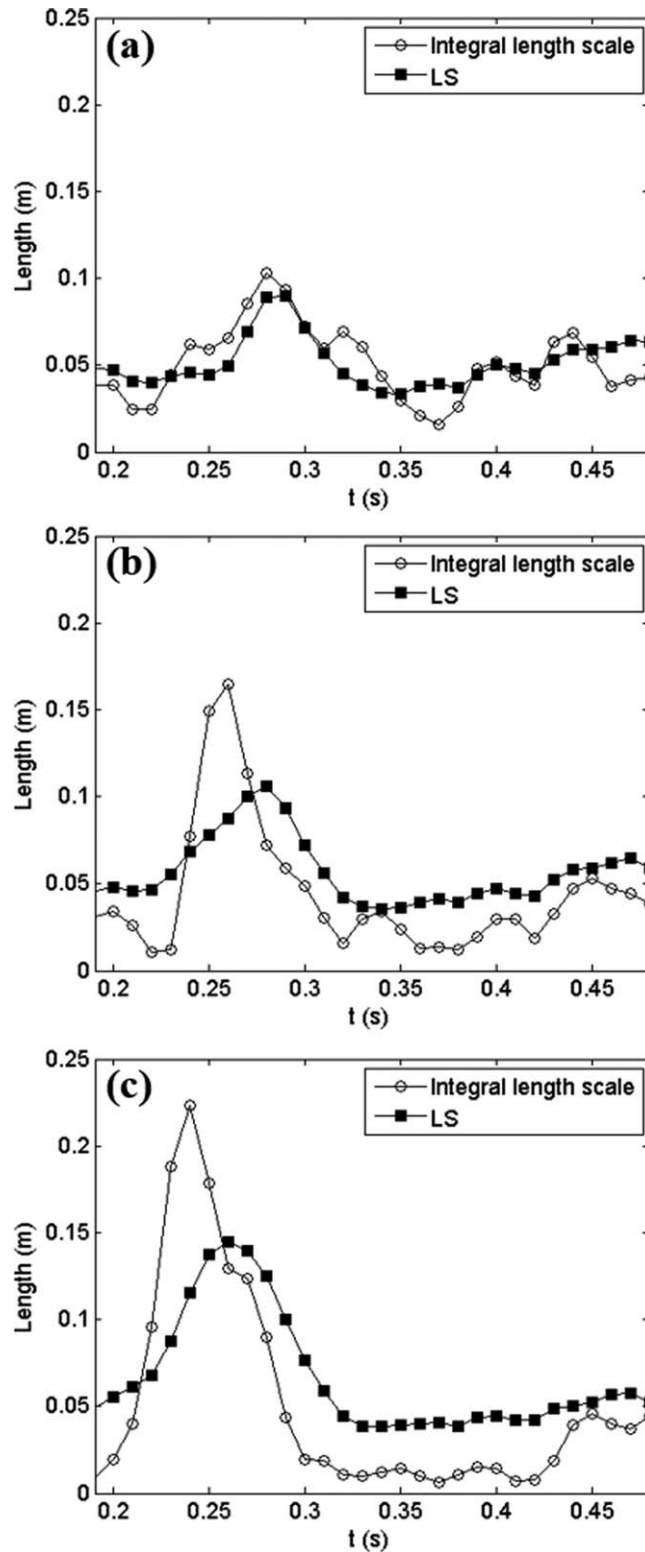


Figure 8. Comparisons between the integral length scale and the wavelet resolved length scale *LS* at *z* = (a) 0.01 m, (b) 0 m, and (c) -0.01 m at FOR station 1 (*x* = 0.43 m).

was first computed, and then was converted to the corresponding length scale by multiplying the phase speed *C* because the horizontal domain covered by each FOV is insufficient for the correlation computation. The integral time scale can be computed as

$$l_t = \int_0^\infty \frac{\langle u'(t+\tau)u'(t) \rangle}{\langle (u'(t))^2 \rangle} d\tau \quad (7)$$

where $u'(t)$ is the horizontal component of turbulent velocity at a given point. Figure 8 shows the comparisons of the wavelet-resolved length scale and the integral length at three different *z* locations at FOR station 1. Note that all the measurement locations are below the free surface over the period chosen, covering the first splash-up roller and the first impinging roller. The length scales do not vary significantly in time and space, except at 0.23 s < *t* < 0.3 s when the ascending crest [see *Lim et al., 2015*] with few bubbles reaches the measurement station. However, the discrepancy between the integral length scale and *LS* becomes larger at the lower measurement points. Since the wavelet-resolved length scale estimate is based on analyzing the horizontal velocity along a vertical column different from the integral length-scale estimate, which is based on the autocorrelation of the horizontal velocity along an equivalent horizontal row, the discrepancy may indicate that the eddies become more elliptical at the lower part of the rollers where shear is greater.

4. Bubble-Size Distribution

The FOR technique was employed to measure the void fraction and bubble-size distribution within the aerated region. Figure 9 shows sample FOR signals taken at station 1 (*x* = 0.43 m). With help from the images recorded by the high speed camera, we are able to relate the FOR signals to the wave breaking process. The probe at the

measurement point encounters several stages of the breaking process, including the first splash-up roller, the ascending crest region, the first backward impingement, and the first impinging roller, as described in

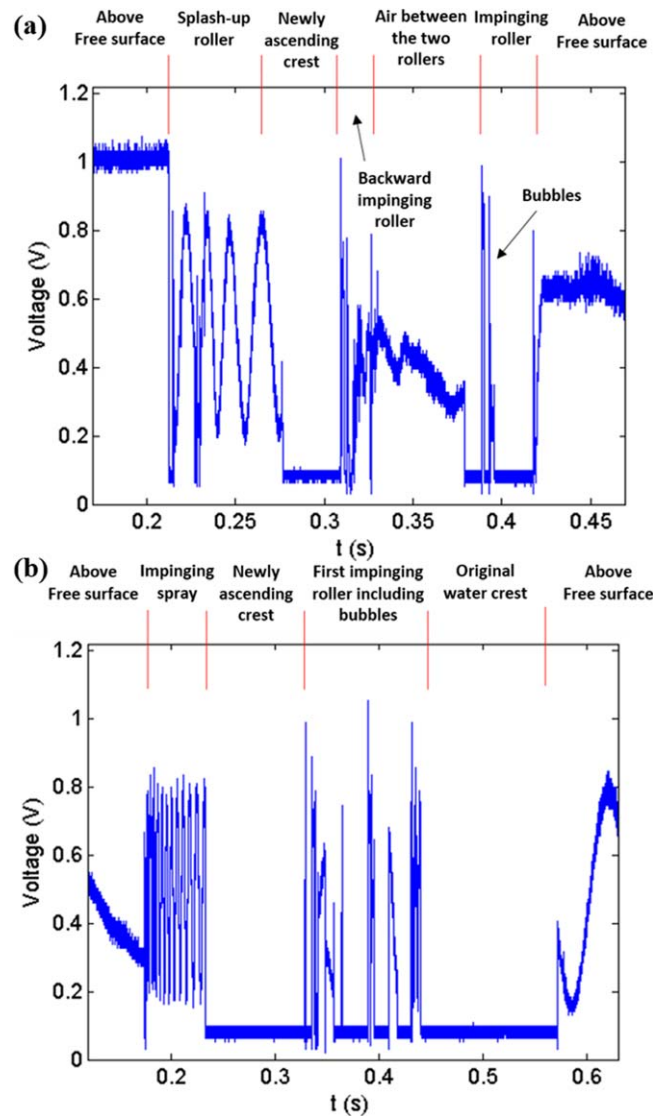


Figure 9. Sample instantaneous FOR signals at station 1 ($x = 0.43$ m) at (a) $z = 0.07$ m (roughly the middle of the first splash-up roller) and (b) $z = 0$ m, with $V > 0.11$ indicating the presence of air.

Lim et al. [2015]. A voltage value of around 0.08 V indicates that the fiber sensor tip is in water, whereas a value around 1.0 V indicates that the tip is in air. However, the higher voltage signals that represent the gas phase do not always remain at 1.0 V because the fiber tip does not dry immediately after it leaves water. The signals fluctuate with a value higher than 0.08 V during the drying process. The voltage difference between the liquid phase and gas phase is highly distinguishable, even though the gas-phase signals fluctuate due to the rapid response of phase change when the probe is leaving water. A threshold value to separate the two phases and determine gas residence time and void fraction was set close to the gas phase (0.11 V in the present study), accounting for the maximum noise level of the liquid-phase signals. The FOR technique has been validated in Chang et al. [2003] and Lim et al. [2008]. Details on void fraction measurements of the present breaking waves using FOR have been reported in Lim et al. [2015].

The FOR signals were analyzed to detect bubbles. A total of 760 sets of FOR measurements (20 repeated runs at each of the 19, 12, and 7 vertical locations at FOR stations 1, 2, and 3, respectively) were performed to obtain the bubble chord length distributions. In the analysis, the phases that corresponded to the passage of the three splash-up rollers at each FOR station were first identified by synchronizing the BIV images and the

corresponding FOR signals. The bubble signals detected only within these phases were considered as bubbles that led to the bubble-size distributions in Figures 12 and 13. Occasionally “wet” signals were detected at a relative distance ahead of the arrival of the splash-up rollers. Such signals were removed due to their likelihood of resembling droplets. However, droplets in close proximity to the splash-up rollers (or inside the rollers) could not be distinguished. Fortunately—for such small-scale breakers—the BIV images showed that few droplets were observed in front of the splash-up rollers, and that a relatively small number of droplets was observed inside the splash-ups when compared to the number of bubbles. This suggests that the influence of droplets may be insignificant, at least for the small-scale laboratory breakers.

The interval when the fiber tip is inside a bubble is measured and defined as the bubble residence time, T_b . Since the PIV and BIV velocity measurements in the highly aerated region are essentially based on bubble displacements, a bubble chord length, s , can be estimated as

$$s = T_b V \tag{8}$$

where V is the mean speed measured using PIV and BIV. To obtain the bubble chord length, both the bubble velocity and residence time must be known. Note that the FOR, BIV, and PIV measurements were not performed simultaneously. This means the FOR signals are instantaneous while the velocities are ensemble-averaged mean values—which indicates that the calculated bubble sizes would have an uncertainty of about 20% due to turbulence fluctuations. Furthermore, the above equation is for chord length estimation rather than the actual bubble-size (i.e., diameter) distribution (because the probe does not always intersect a bubble at its center). To convert from a chord length distribution to the equivalent size distribution, a statistical correction is needed. Although *Clark and Turton* [1998], *Liu and Clark* [1995], and *Liu et al.* [1996] provided methods to convert the bubble diameter distribution from a chord length distribution based on probabilistic analysis, applying their methods was not successful in the present study (especially at the upper and lower extremes of the size distribution) because of the complex flow condition. Alternatively, *Serdula and Loewen* [1998] and *Rojas and Loewen* [2007] suggested a simple average correction factor of 3/4 to convert the measured chord length to bubble radius following the analysis of *Saberi et al.* [1995]. The uncertainty due to the use of the average correction factor may be estimated as the standard deviation of the measured chord lengths from the averaged chord length, $\sigma^2 = \int_0^r (s - \bar{s})^2 P(x) dx$, where r is the radius of bubble, $s = \sqrt{r^2 - x^2}$ is the measured chord length, $\bar{s} = 4r/3$ is the average chord length, and $P(x)$ is the probability density function. The calculated standard deviation is about $0.47r$ or 24% of the bubble diameter.

In the present study, the total number of bubbles ($s > 0.125$ mm) detected is 2569, 1111, and 656 at FOR station 1, 2, and 3, respectively. *Clark and Turton* [1998] suggested that bubbles with a diameter smaller than the probe diameter will resist piercing unless the bubble velocity is very high. Since the chord length is always less than the diameter of a bubble, the measured chord lengths shorter than the diameter of the FOR probe of 125 μm were not included in the bubble-size distribution. The results show that bubbles with a chord length $s < 2$ mm (defined as “smaller bubbles” hereafter) account for 42% of all the bubbles detected during the first splash-up process at FOR station 1. A similar percentage of smaller bubbles was found during the second and the third splash-ups at FOR stations 2 and 3 (although the total numbers of bubbles detected was significantly lower). Using $s = 2$ mm to separate bubbles into two groups is justified by the Hinze scale [*Deane and Stokes*, 2002] that is discussed in the following sections.

Figure 10 shows the spatial distributions of the bubble chord lengths at the three FOR stations plotted as histograms. At FOR station 1, more than 85% of the smaller bubbles (i.e., $s < 2$ mm) were found above the still water level (SWL) as shown in Figure 10a, indicating that the majority of the smaller bubbles were created by the impact and the subsequent splashing up in the wave breaking process. On the other hand, larger bubbles are more uniformly distributed over the vertical water column. *Deane and Stokes* [2002] suggested two distinct flow features that drive bubble creation in breaking waves: smaller bubbles are created by the impact and subsequent splashing, while larger bubbles are created by the collapsing air cavity. This is because bubble break-up, or fragmentation, occurs when the differential pressure force associated with turbulence exceeds the restoring force of surface tension [*Hinze*, 1955]. *Deane and Stokes'* bubble creation mechanism is consistent with the observation in the present study. At FOR station 2, the number of larger bubbles decreases to about one half of that at FOR station 1. At FOR station 3, the number of larger bubbles continues to decrease to about one fifth of that in the first splash-up, and they (i.e., these larger bubbles) were observed to burst on the free surface (based on the BIV images).

Figure 11 shows the vertical distributions of the number of smaller and larger bubbles measured during the passage of the splash-up roller (Figures 11a and 11b) and the impinging roller (Figures 11c and 11d) at FOR station 1. The swirling strength, averaged over the corresponding “bubble generation” stage, was also plotted for comparison. By identifying the phases that correspond to the passage of different rollers at FOR station 1, bubbles generated by the first splash-up roller were distinguished from those generated by the first impinging roller (i.e., bubbles generated from the fragmentation of the air cavity). During the passage of the impinging roller, the distribution of smaller bubbles shows good correlation (correlation coefficient $r = 0.72$) with the swirling strength (Figure 11c), whereas the correlation is weaker ($r = 0.56$) for the larger bubbles (Figure 11d). The results imply that the local swirling motion of the energetic eddies, and the associated differential pressures acting on the bubbles, enhance the breakup of the larger bubbles into smaller bubbles. Thus the distribution of swirling strength and the number of smaller bubbles are clearly correlated. On the other hand, during the passage of the first splash-up roller (Figures 11a and 11b), the swirling strength shows much weaker correlation with the number of bubbles generated during the process. The

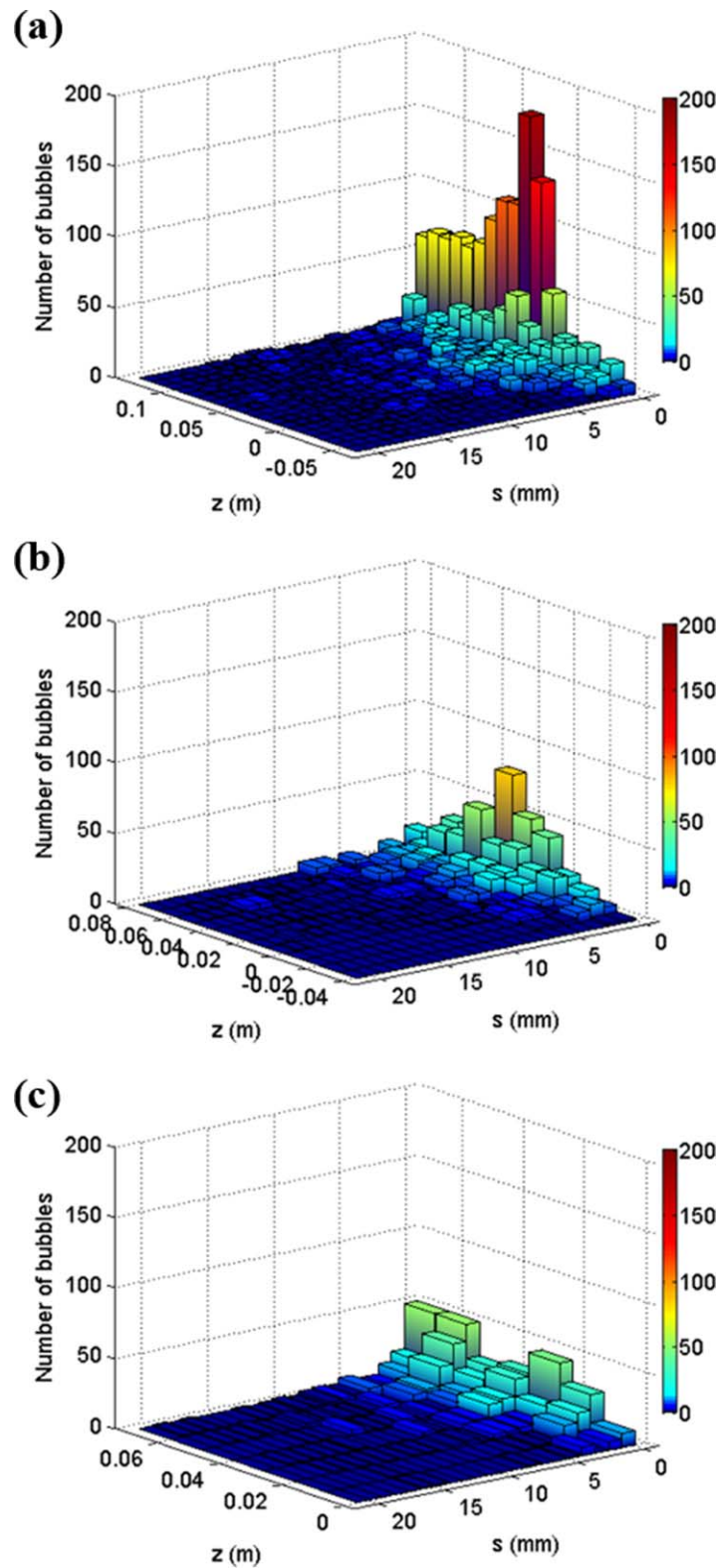


Figure 10. Histograms of chord length distributions at (a) FOR station 1, (b) FOR station 2, and (c) FOR station 3.

distinct power-law scaling relationships during the passage of the first impinging roller. On the contrary, Figure 12b does not clearly show distinct slopes during the passage of the first splash-up roller. For the bubbles

results suggest that the local swirling motion that causes bubble break-up, as shown in Figures 11c and 11d, is not the dominant mechanism for bubble creation in the first splash-up roller. Note that the number of bubbles generated in the first splash-up roller is not significantly different from that generated in the first impinging roller, except for with the smaller bubbles ($s < 2$ mm) at $z=0.01$ m and $z=0.02$ m (as shown in Figure 11a). In these elevations, high shear occurred due to the differential motion between the high-speed rotation in the first splash-up roller and the low-speed wave motion under the trough level.

Figure 12 shows the probability density function (PDF) of bubble size measured at FOR station 1 during the passage of the first impinging roller (Figure 12a) and the splash-up roller (Figure 12b). Bubbles in these two rollers are analyzed separately because of their distinct behavior. The PDF is defined as

$$P(x, s)ds = \frac{1}{N} \sum_z N_s(x, z, s) \Delta s \tag{9}$$

where P is the PDF, N is the total number of measured bubbles within one wave period, N_s is the number of bubbles per wave period at a particular measurement location (x, z) (i.e., the 19, 12, and 7 points at FOR stations 1, 2, and 3, respectively) with a particular bubble size (s) , and Δs is the bin size. The bubble-size distribution is, in general, represented as the bubble count per unit volume. Since the measurement volume is not well defined in the present study, it is simply plotted as a PDF. Figure 12a shows two

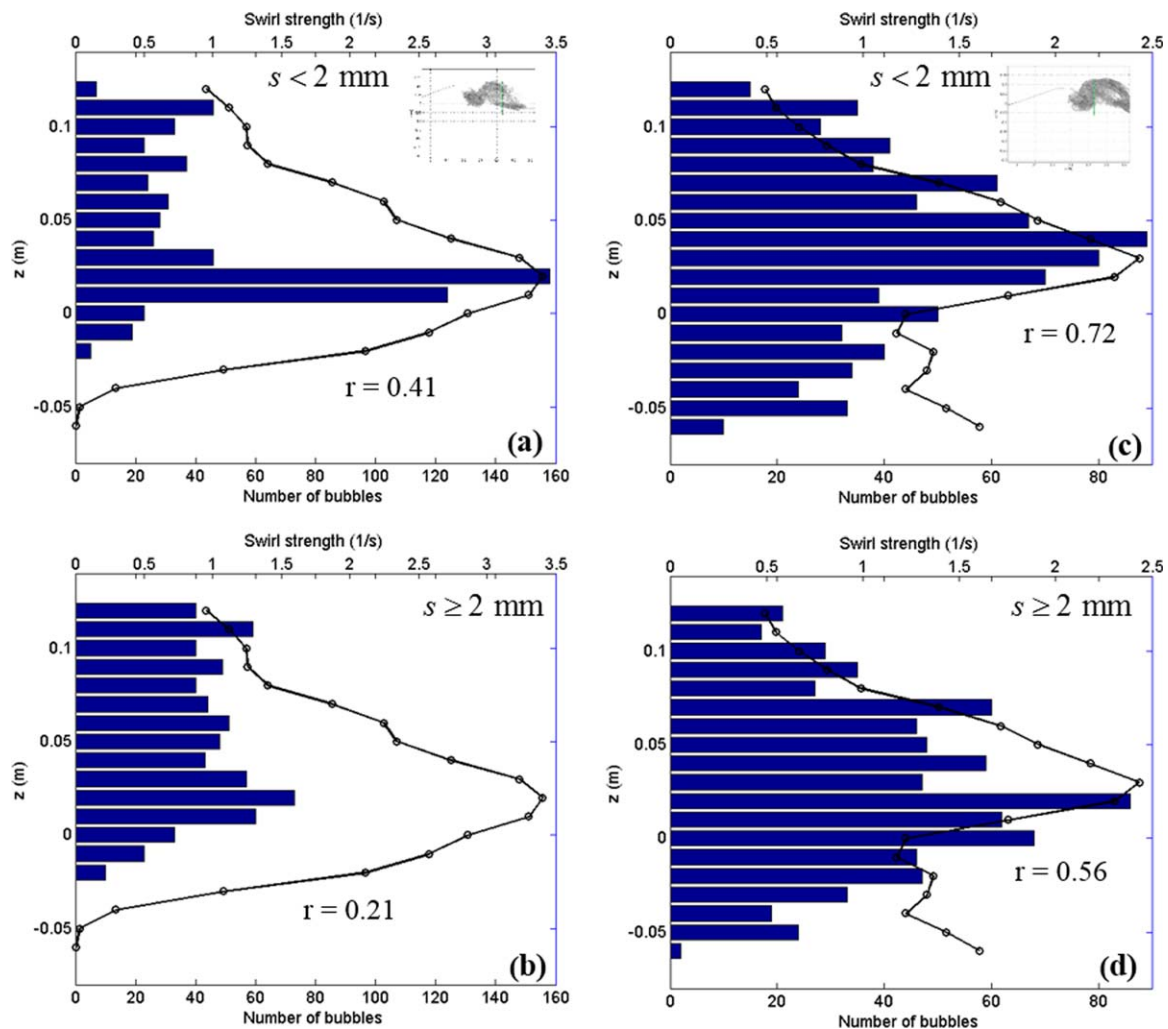


Figure 11. Vertical distributions of the number of bubbles with a chord length of $s < 2$ mm (a, c) and $s \geq 2$ mm (b, d) measured during the passage of the splash-up roller (a, b) and the impinging roller (c, d) at FOR station 1. The insets illustrate the measurement locations at the two rollers. The lines indicate the vertical distribution of stage-averaged swirling strength. No bubbles were detected below $z < -0.02$ m in the splash-up roller. The r value denotes the correlation coefficient between the number of bubbles and the corresponding swirling strength.

associated with the impinging roller (Figure 12a), the two slopes are $\Phi_{1f} = -0.9$ and $\Phi_{2f} = -2.9$ —with a slope change occurring at about $s = 3.0$ mm for both. *Deane and Stokes* [2002] used video recordings to obtain the bubble-size distribution in breaking waves in seawater. They found that the distinct change of the two slopes ($\Phi_1 = -1.5$ and $\Phi_2 = -3.3$ in their study) occurred for bubble radii larger than approximately 1–2 mm, and they defined that scale as the “Hinze scale” [Hinze, 1955]. Since our data are based on the chord length distribution, if the average conversion factor of 3/4 (between the chord length and the radius) is applied, the Hinze scale (in radius) becomes $a_H = 2.3$ mm which is close to what Dean and Stokes found. The reason for the discrepancy between the power-law scaling and the Hinze scale may be attributed to the fact that the use of seawater in Deane and Stokes leads to an increase of the surface tension. Moreover, the difference may also be attributed to calculating the bubble size/frequency between images and FOR. The FOR system determines the chord lengths of bubbles that penetrate through the miniature tip of the probe (125 μm in diameter)—so only bubbles that encountered the probe tip were recorded. It is possible that smaller bubbles, which might not be accounted for in the current study, were included in *Deane and Stokes* [2002]—and thus explain the decreased steepness of the slope Φ_1 (in the present study).

Despite the results showing that the slope for smaller bubbles is flatter, the slope for larger bubbles and the Hinze scale in the present study are consistent with the values previously reported by *Deane and Stokes* [2002], *Rojas and Loewen* [2007], and *Mori and Kakuno* [2008]. Using a dual-tip fiber probe in plunging breaking waves,

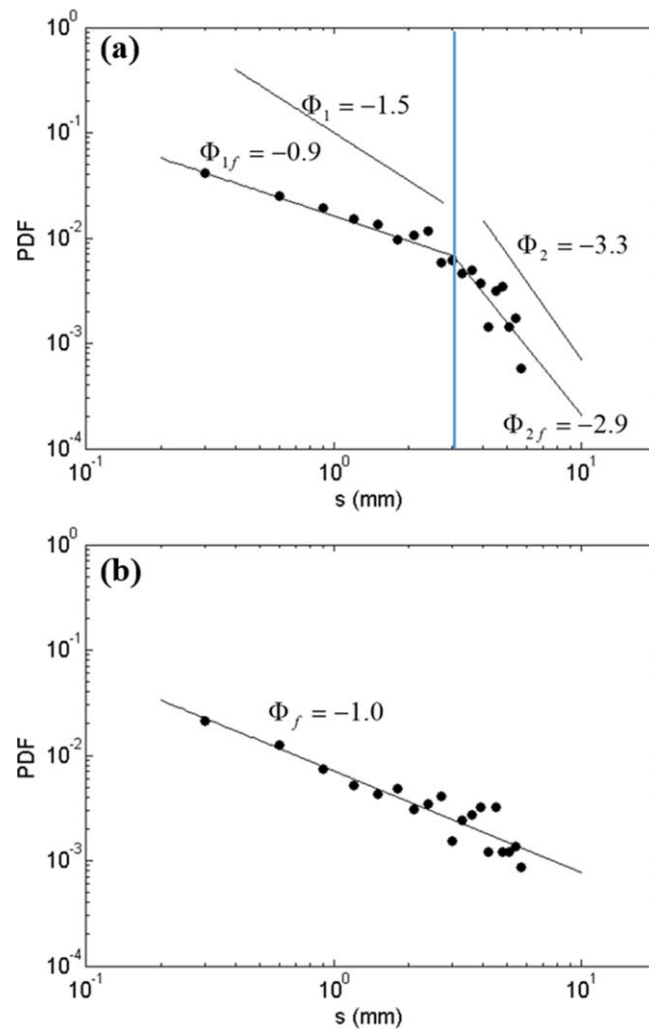


Figure 12. The bubble-size distributions at FOR station 1 during the passage of (a) the impinging roller ($t = 0.3\text{--}0.7$ s), and (b) the splash-up roller ($t = 0\text{--}0.3$ s). The lines in Figure 12a are least-square fits (with exponents of Φ_{1f} and Φ_{2f}), and power-law scaling lines from *Deane and Stokes* [2002] (with exponents of Φ_1 and Φ_2) are shown for comparison. The vertical line at the slope change denotes the Hinze scale. The line in Figure 12b is the least-square fit of the measurement data.

bles in the splash-up roller is not steep compared with that in the case of the impinging roller in Figure 12a. This may indicate that larger bubbles initially entrained in the splash-up roller remained close to the surface in the roller, leading to a relative large number of larger bubbles. These larger bubbles may move upward and burst out of the free surface, or may move downward and break up due to the strong swirling motion (as they move deeper). In either case the result is a smaller number of larger bubbles at depth. Similarly, *Baldy* [1988], *Rojas and Loewen* [2007], and *Blenkinsopp and Chaplin* [2010] observed that the slope of the larger bubbles becomes steeper with depth in the impinging roller. Direct comparisons between their observations and the present study are not possible due to an insufficient number of bubbles at each depth in the present study. However, their observations are consistent with the bubble-size distribution in the splash-up roller in the present study. Even though the turbulence intensity is very high in the splash-up roller [*Lim et al.*, 2015], bubble break-up does not occur as frequently as it does in the impinging roller (in Figure 12a), leading to a flatter slope in Figure 12b. The cause is not clear, but the very high void fraction in the first splash-up roller [*Lim et al.*, 2015] is likely involved.

Figure 13 shows the PDF of bubble sizes at FOR stations 2 and 3. In Figure 13a, the two power-law scaling relationships ($\Phi_{1f} = -0.9$, $\Phi_2 = -2.9$) and the Hinze scale ($a_H \sim 2.8$ mm) at FOR station 2 are shown. These values are similar to those found at FOR station 1 for the impinging roller ($\Phi_{1f} = -0.9$, $\Phi_{2f} = -2.9$, and a_H

Rojas and Loewen [2007] suggested a radius of 1.5 mm for the Hinze scale and power-law scaling of $\Phi_1 = -1.5$ and $\Phi_2 = -3.0$. They measured bubble sizes at 1.5 cm below the SWL with repeated breaking waves. *Mori et al.* [2007] found a Hinze scale of 2.0 and 4.3 mm in their small-scale and large-scale experiments, respectively, and power-law scaling of $\Phi_1 = -1.5$ and $\Phi_2 = -1.7$. *Mori and Kakuno* [2008] used an imaging technique to measure the bubble sizes and found a Hinze scale of 3.0 mm and power-law scaling of $\Phi_1 = -1.0$ and $\Phi_2 = -3.4$ for surf zone breaking waves.

The distribution of bubbles within the splash-up roller does not show a distinct change of slope throughout the entire range of bubble sizes (Figure 12b). It was observed from the images, and the corresponding FOR signals, that the splash-up roller consists of water droplets and air bubbles induced by the upward momentum due to the impact and splash up of the overturning jet. Few measurements of bubble size in the first splash-up roller were reported since most of the previous studies were mainly concentrated on bubbles located close to, or below, the SWL [e.g., *Serdula and Loewen*, 1998; *Rojas and Loewen*, 2007; *Mori et al.*, 2007; *Blenkinsopp and Chaplin*, 2010]. As far as the authors know, this is the first estimate of the bubble-size distribution in the splash-up roller in plunging breaking waves. This makes direct comparisons infeasible. In Figure 12b, the slope of the larger bubbles

in the splash-up roller is not steep compared with that in the case of the impinging roller in Figure 12a. This

may indicate that larger bubbles initially entrained in the splash-up roller remained close to the surface in the roller, leading to a relative large number of larger bubbles. These larger bubbles may move upward and burst out of the free surface, or may move downward and break up due to the strong swirling motion (as they move deeper). In either case the result is a smaller number of larger bubbles at depth. Similarly, *Baldy* [1988], *Rojas and Loewen* [2007], and *Blenkinsopp and Chaplin* [2010] observed that the slope of the larger bubbles becomes steeper with depth in the impinging roller. Direct comparisons between their observations and the present study are not possible due to an insufficient number of bubbles at each depth in the present study. However, their observations are consistent with the bubble-size distribution in the splash-up roller in the present study. Even though the turbulence intensity is very high in the splash-up roller [*Lim et al.*, 2015], bubble break-up does not occur as frequently as it does in the impinging roller (in Figure 12a), leading to a flatter slope in Figure 12b. The cause is not clear, but the very high void fraction in the first splash-up roller [*Lim et al.*, 2015] is likely involved.

Figure 13 shows the PDF of bubble sizes at FOR stations 2 and 3. In Figure 13a, the two power-law scaling relationships ($\Phi_{1f} = -0.9$, $\Phi_2 = -2.9$) and the Hinze scale ($a_H \sim 2.8$ mm) at FOR station 2 are shown. These values are similar to those found at FOR station 1 for the impinging roller ($\Phi_{1f} = -0.9$, $\Phi_{2f} = -2.9$, and a_H

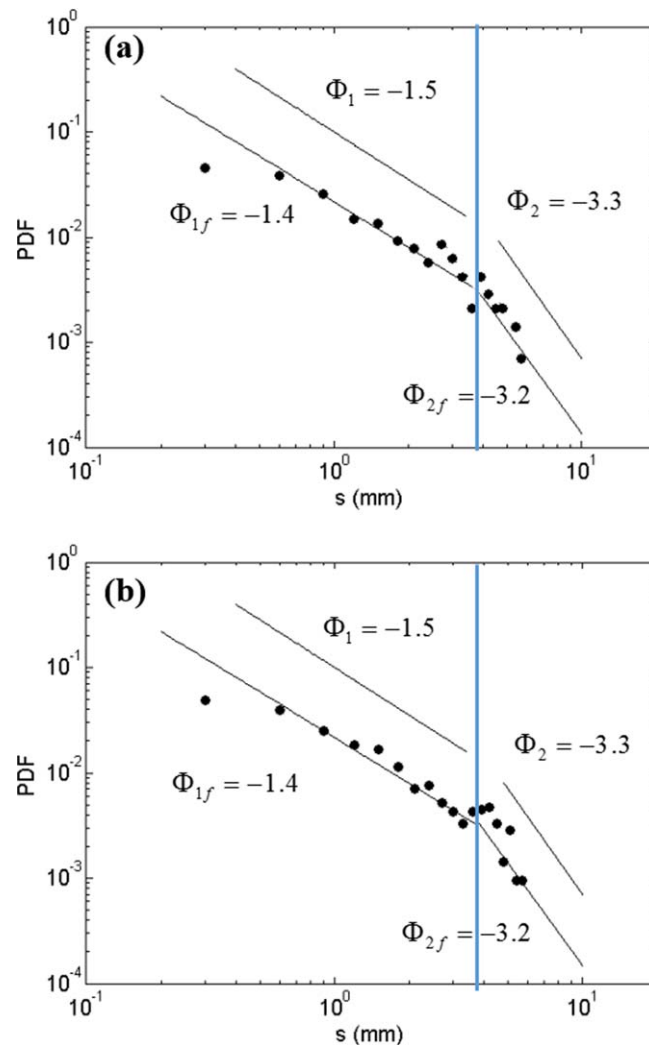


Figure 13. The bubble-size distributions at (a) FOR station 2 and (b) FOR station 3. The lines are least-square fits (with exponents of Φ_{1f} and Φ_{2f}) and power-law scaling lines from Deane and Stokes [2002] (with exponents of Φ_1 and Φ_2) are shown for comparison. The fitted lines for Figure 13a are used in Figure 13b due to an insufficient number of bubbles. The vertical line at the slope change denotes the Hinze scale.

have already been performed in the present study. As mentioned in Lim *et al.* [2015], the authors spent more than one year to complete the data collection (when including initial trial tests used to optimize the instrumentation and data acquisition), and then a few more years for data analysis and summarizing the findings. Even though the number of bubbles detected in the present study is insufficient to result in a spatial distribution of bubble sizing, the reasonably large numbers of total detected bubbles (2569, 1111, and 656 at FOR station 1, 2, and 3, respectively) seem to be enough for the depth-integrated analysis. The number of bubbles detected at FOR station 1 is indeed comparable to that used for calibration under plunging breaking waves by Rojas and Loewen [2010]. The findings presented in the figures—even though not as smooth as one would expect to see for converged results—seem to be sufficient to interpret the underlying physics.

5. Effects of Void Fraction to Energy Dissipation

Energy dissipation in the active breaking zone of a breaking induced two-phase flow is one of the least understood parts in the study of wave breaking. Great efforts and progress have been made in the study of bubble entrainment and evolution under breaking waves both numerically [e.g., Ma *et al.* 2011; Derakhti

~ 2.3 mm), as shown in Figure 12a. This similarity of bubble-size distribution implies that the bubble formation process is similar between the first impinging roller and the second impinging and splash-up rollers, in which the splash-up is rather weak. The same power-law scaling at FOR station 2 was directly applied to the bubble-size distribution at FOR station 3, as shown in Figure 13b, due to an insufficient number of bubbles for a reasonable regression fit. The weak turbulence level (less than one half of that at FOR station 2) may lead to less bubble break-up events, in addition to bubbles bursting at the free surface during that breaking stage.

Blenkinsopp and Chaplin [2007] presented void fraction estimates in breaking waves using an optical fiber system, and they used between 200 and 400 waves at each measurement location to ensure stable void fraction estimates. In comparison, only 20 repeats at each FOR measurement point were performed for ensemble averaging in the present study. The number of repeats is obviously insufficient to result in converged void fraction estimates, and is insufficient for bubble counting and sizing. However, this is a unique study that measured both void fraction and velocity fields. Repeating more than 20 times for each of the 38 FOR measurement points is impractical considering that a total number of 1120 repeated measurements (760 for FOR, 340 for PIV and BIV combined, and 20 for wave gauges)

and Kirby, 2014] and experimentally [e.g., Cox and Shin, 2003; Mori et al., 2007; Blenkinsopp and Chaplin, 2010]. However, experimental results are mostly based on void fraction or turbulence measurements. The relation between the two—probably due to the difficulties in measuring both void fraction and velocity in the highly aerated flow—has rarely been reported. Void fraction can be used to quantify the mixture density, which in turn can be applied to estimate both the liquid-phase wave energy and dissipation in plunging breaking waves [Lim et al., 2015]. In this section, we expanded Lim et al.'s study to quantify the turbulent dissipation rate—both with and without considering the void fraction—and relate the turbulent dissipation rate to the total energy dissipation rate. Turbulence dissipation featuring the dispersed phase in breaking waves has rarely been reported in experimental studies. Here we also discussed the turbulence dissipation rate by dispersed bubbles, and the role it plays in energy balance in the wave breaking process.

5.1. Estimation and Comparison of Turbulent Dissipation Rate

For a flow with a balanced turbulence kinetic energy production and dissipation, the turbulence dissipation rate can be estimated from the Kolmogorov $-5/3$ spectral slope in the inertial subrange of the velocity spectrum. Using the isotropic assumption, the spectra E and the turbulent dissipation rate ε in the inertial subrange have the following relationship [Tennekes and Lumley, 1972]:

$$E(\kappa) = \frac{18}{55} \beta \varepsilon^{2/3} \kappa^{-5/3} \tag{10}$$

where $\beta=1.5$ is the universal Kolmogorov constant and κ is the wavenumber along the horizontal (stream-wise) direction. In the present study, the wave number spectra of each row of the measured velocity field were ensemble-averaged and then wave-averaged to estimate the time-averaged turbulence dissipation rate. The wave-averaged quantity f_{wa} (wet-period averaged) and the period-averaged quantity \bar{f} (averaged over one-wave period) for a variable f at a given point are defined as

$$f_{wa}(x, z) = \frac{\int_{t_{tr}(x,z)}^{t_{tr}(x,z)+T} \delta(x, z, t) f(x, z, t) dt}{\int_{t_{tr}(x,z)}^{t_{tr}(x,z)+T} \delta(x, z, t) dt} \tag{11}$$

$$\bar{f}(x, z) = \frac{\int_{t_{tr}(x,z)}^{t_{tr}(x,z)+T} \delta(x, z, t) f(x, z, t) dt}{\int_{t_{tr}(x,z)}^{t_{tr}(x,z)+T} dt} \tag{12}$$

where $t_{tr}(x, z)$ is the time when the front trough reaches a specific measurement point. $\delta(x, z, t)=1$ when the point (at time t) is in the water, and $\delta(x, z, t)=0$ otherwise. Only the wetted region is considered in the calculation of wave-averaged quantities, while the period-averaged values are obtained from the summation of quantities divided by the corresponding local wave period.

Figure 14 shows the wave-averaged wave number spectra of horizontal velocity fluctuations at various depths. Based on measurements in FOV5 that feature the initial impinging and the first splash-up roller, the spectra decay less rapidly when ($\kappa < 70$ rad/m), more rapidly when close to ($70 < \kappa < 170$ rad/m), and again less rapidly when ($\kappa > 170$ rad/m). The ranges of the estimated inertial subrange, and the three stages, are similar to those reported by Drazen and Melville [2009] and Govender et al. [2004] for the post breaking velocity field and surf-zone spilling breakers, respectively. The inertial subrange typically extends from the size of large eddies, which can be determined by the physical dimensions of the flow (e.g., the wave height) relative to the Kolmogorov microscale. The vertical size of the first splash-up roller yields $\kappa \sim 42$ rad/m (or 0.15 m) for the lower limit of the inertial subrange, and our estimation of $\kappa < 70$ rad/m is in reasonable agreement. The dissipation rate in the current study roughly ranges from 10^{-4} to 10^{-3} m^2/s^3 , resulting in a Kolmogorov microscale $\eta=(\nu^3/\varepsilon)^{1/4}$ of about 0.1 mm—which is about one order of magnitude smaller than the spatial resolution of the current velocity measurements. The less rapid decay of the spectrum in the larger wave number region in the present study was also observed in previous wave breaking studies [Govender et al., 2004; Drazen and Melville, 2009]. Doron et al. [2001], and Nimmo Smith et al. [2005] reported that this less rapid decay rate is due to the build-up of energy near the border between the inertial subrange and the dissipation range. Another interesting feature in Figure 14 is that the number of

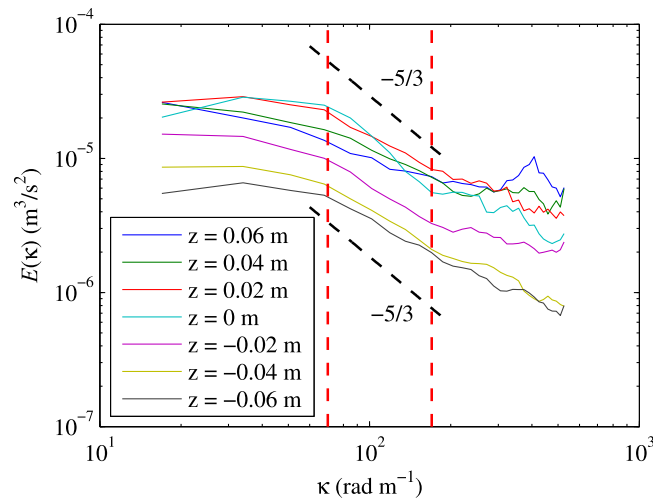


Figure 14. Wave-averaged wave number spectra at different vertical locations. The region between the two dotted lines ($70 < \kappa < 170$ rad/m) is referred to as the inertial subrange for comparison with the Kolmogorov $-5/3$ scaling. All the slopes are flatter than $-5/3$ except the one for $z = 0$ m.

including that based on the spectrum analysis and that from the measured velocity fields (as stated in Doron *et al.* [2001] and detailed in the Appendix A). The turbulent dissipation rate ε_{LF} was computed from the wave number spectrum based on equation (10) using least-square fits over the inertial range ($70 < \kappa < 170$ rad/m) where the $-5/3$ slope was found. Figure 15 shows the vertical profiles of the estimated wave-averaged turbulent energy dissipation rate using five different methods at FOR stations 1–3. All the estimates are of the same order-of-magnitude and do not differ significantly. The ε_D values obtained from the “direct” estimate [Doron *et al.*, 2001] are greater than those of the other four estimates. This is likely caused by the assumption that the lateral fluctuations are of similar magnitude as the streamwise fluctuations. In Figure 15a, the high dissipation rate is concentrated within the aerated region above the trough level, indicating that strong turbulence is generated in the impinging and splash-up roller region at FOR station 1 (see Figure 6d for comparison). The dissipation rate follows an exponential decay below the lower boundary of the splash-up roller ($z \sim -0.03$ m). The peak dissipation rate occurs near the SWL, and coincides with the condensed high intermittency and vorticity (as shown in Figure 6d). At FOR station 3, ε_D shows a similar level of magnitude in estimating ε as compared with using other methods. This implies that the isotropic assumption may not be much of an issue when the maximum wave-averaged void fraction is small (~ 0.32) compared to the value of 0.6 at FOR station 1 [see Lim *et al.*, 2015, Figure 13a]. The dissipation rate at FOR station 3 is reduced to about only 10% of that at FOR station 1. The turbulence dissipation rates below the lowest limit of the aerated region at FOR stations 2 ($z \sim -0.04$ m) and 3 ($z \sim 0$ m) follow an exponential decay pattern, similar to that in the spilling breakers reported by Ting and Kirby, [1996], Govender *et al.* [2004], and Huang *et al.* [2009].

In the later analysis, ε_D was chosen to present ε because it may be the most straightforward method that involves the least number of assumptions. It features all the measured gradients (which is not the case for ε_A), less empirical assumptions for the empirical relation (as in estimating ε_C and ε_E), and no assumptions about isotropic turbulence in the inertial range (as in estimation ε_{LF}). Another reason of choosing ε_D was because it led to the lowest excess energy dissipation (i.e., energy dissipation due to sources other than continuous-phase turbulence) and the least discrepancy for the estimated bubble-induced dissipation in the present study (to be discussed later).

5.2. Turbulent Dissipation Rate Considering Void Fraction

Implementing a two-phase (gas-liquid) model in breaking wave studies has not been practical, nor has it been widely reported. However, the multiphase nature is essential in determining energy dissipation in the active breaking region, especially in plunging breaking waves featuring high air entrainment. The dispersed bubbles entrained by waves breaking have intense interactions with the mean flow and turbulence, and produce complex two-phase bubbly flows. For example, it is well known that the presence of bubbles can suppress liquid-

bubbles and the steepness of the slope seem to be related. The slopes near the inertial subrange are less steep above the SWL compared to that below the SWL, whereas the numbers of bubbles detected above the SWL are greater than that below the SWL, as shown in Figure 10. Similarly, Rensen *et al.* [2005] observed a milder slope for a two-phase bubbly flow, in comparison to that for a grid generated single-phase turbulent flow. That implies the energy increase at the smaller length scale is caused by the direct forcing through the bubbles, while the reduction of the energy at the larger length scales is caused by bubble accumulation.

The turbulent energy dissipation rate is estimated using several approaches,

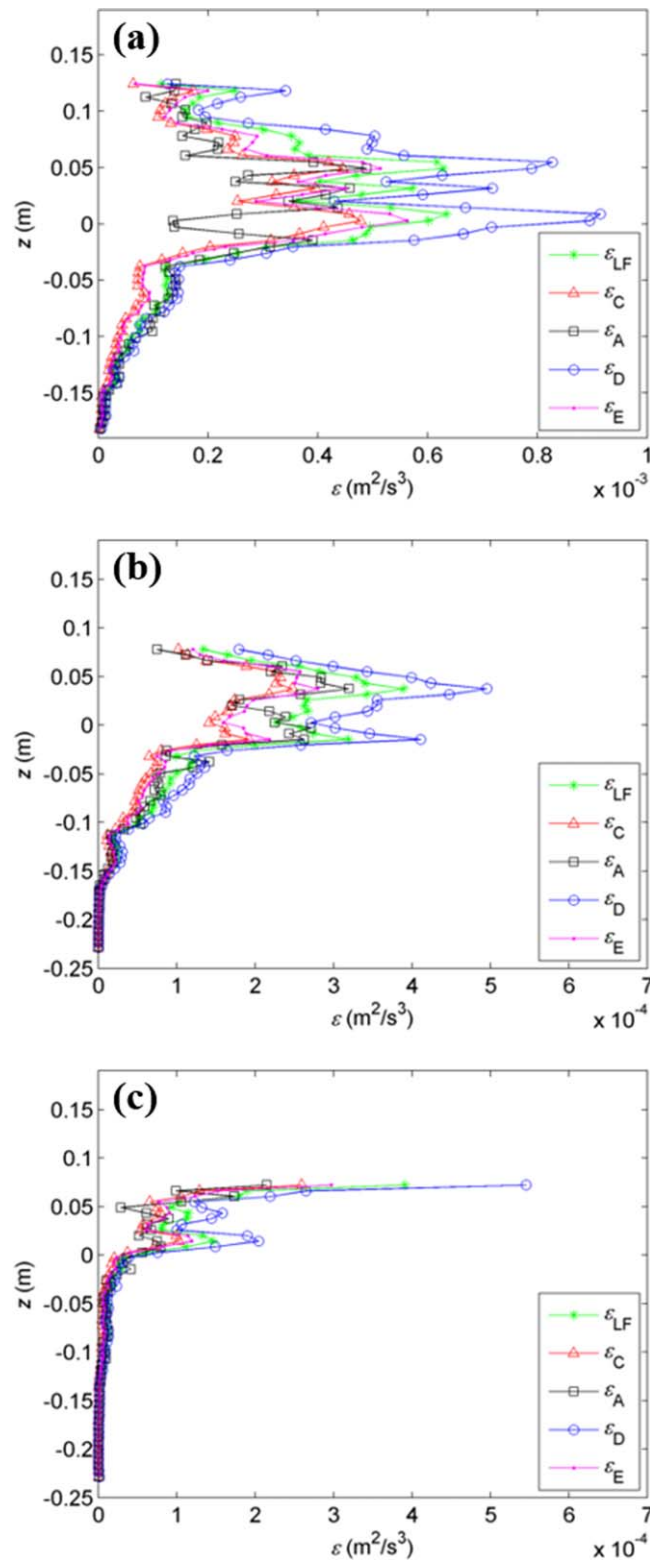


Figure 15. The wave-averaged turbulence dissipation rate, ϵ , estimated using five different methods at (a) FOR station 1, (b) FOR station 2, and (c) FOR station 3. Details of the Methods are stated in Appendix A.

the high values of ϵ_m occur near the lower boundary of the splash-up rollers. The distributions reflect the fact that the fluctuation level is higher with the presence of a high velocity gradient or shear, as shown in *Lim et al.* [2015],

phase turbulence [*Wang et al.*, 1987; *Serizawa and Kataoka*, 1990; *Ma et al.*, 2011] while the turbulent coherent structures generated by breaking can enhance the bubble entrainment [*Baldy*, 1993; *Ma*, 2012]. To calculate the liquid-phase turbulent dissipation rate, void fraction measurements were used to modulate the mixture viscosity based on mixture theory [*Ishii and Mishima*, 1984; *Manninen et al.*, 1996]. In a two-phase bubbly flow, the mixture density can be written as

$$\rho_m = \rho_a \langle \alpha \rangle + \rho_w (1 - \langle \alpha \rangle) \approx \rho_w (1 - \langle \alpha \rangle) \quad (13)$$

where the subscripts a , w , and m represent air, water, and air-water mixture, respectively, and α is the local void fraction. The mixture viscosity model [*Ishii and Zuber*, 1979] can be employed to estimate the dynamic viscosity of bubbly flows. It extends the linear relationship between the mixture viscosity and the continuous phase fluid viscosity to an empirical power relation as follows

$$\frac{\mu_m}{\mu_c} = (1 - \langle \alpha_d \rangle)^{-2.5 \frac{\mu_d + 0.4\mu_c}{\mu_d + \mu_c}} \quad (14)$$

where the subscripts c and d denote continuous phase (water) and dispersed phase (air). Since $\mu_d \ll \mu_c$, the power term $-2.5(\mu_d + 0.4\mu_c)/(\mu_d + \mu_c) \approx -1$. Therefore, the turbulent dissipation rate in a bubbly flow can be formulated as

$$\epsilon_m = \epsilon_w (1 - \langle \alpha \rangle)^{-1} \quad (15)$$

where ϵ_m and ϵ_w denote the turbulent dissipation rate of the air-water mixture (two-phase) flow and the water (single-phase) flow, respectively.

Figure 16 shows the vertical distributions of the wave-averaged turbulence dissipation rate ϵ_D with (denoted as ϵ_m) and without (denoted as ϵ_w) considering void fraction at the three FOR stations. Among the three FOR stations, a somewhat similar trend is observed even though the magnitudes are quite different. Evidently,

the high values of ϵ_m occur near the lower boundary of the splash-up rollers. The distributions reflect the fact that the fluctuation level is higher with the presence of a high velocity gradient or shear, as shown in *Lim et al.* [2015],

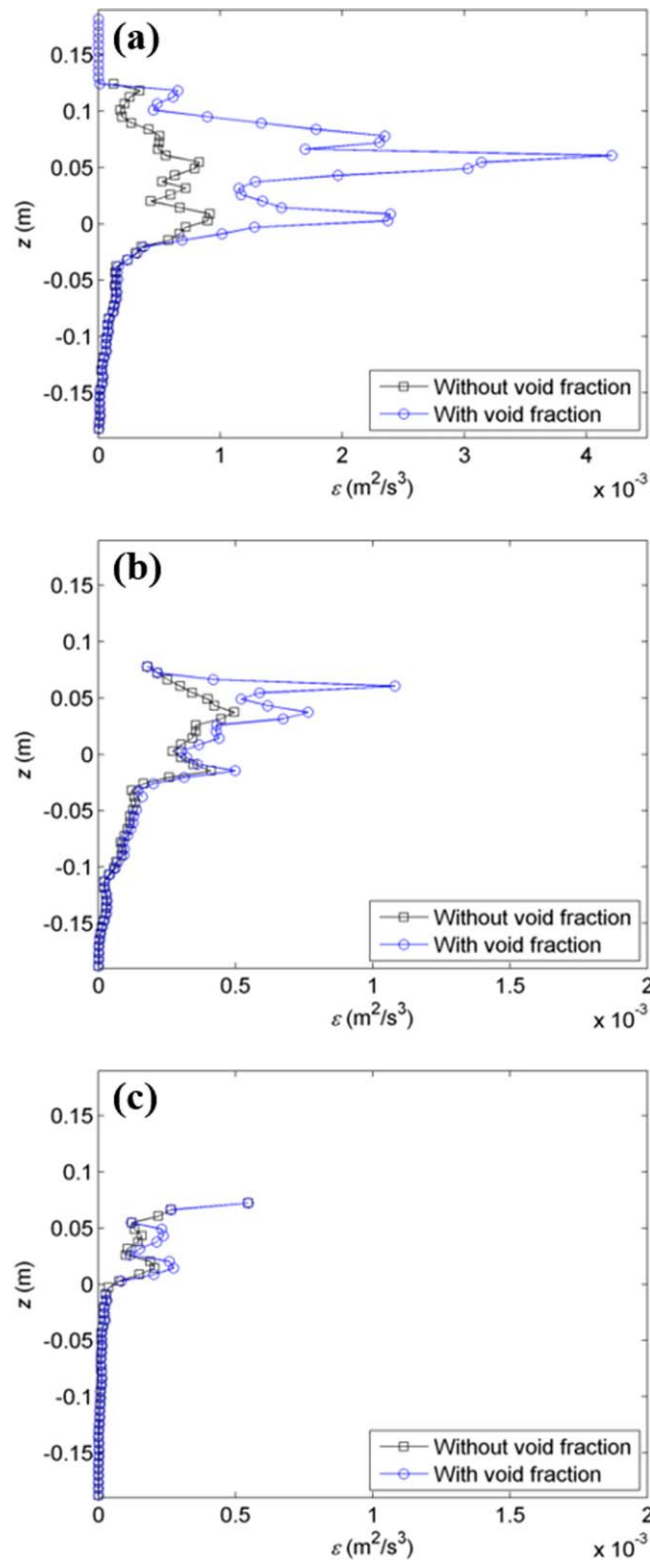


Figure 16. Vertical profiles of the wave-averaged turbulent dissipation rate, ε_D , with and without considering void fraction at (a) FOR station 1, (b) FOR station 2, and (c) FOR station 3.

and becomes lower below the aerated region. To examine the effects of void fraction, the figure shows that ε_w is only 30%, 66%, and 88% of ε_m when integrated with respect to z at FOR stations 1, 2, and 3, respectively, due to the difference in the void fraction level. The maximum values of wave-averaged void fraction occur at the top of the wave crest, reaching 0.57, 0.49, and 0.32 at FOR stations 1, 2, and 3, respectively [Lim *et al.*, 2015]. The discrepancy is significantly smaller at the third splash-up (FOR station 3) when compared with that at the first two splash-ups. The results indicate that the presence of bubbles plays a prominent role in enhancing the turbulent dissipation rate, especially with a void fraction over 0.5. Similarly, the presence of bubbles can suppress liquid-phase turbulence [Wang *et al.*, 1987; Serizawa and Kataoka, 1990; Ma *et al.*, 2011], change the local vorticity, and eventually deform or displace vortex structures [Watanabe *et al.*, 2005]. Ma *et al.* [2011] simulated turbulence dissipation rates and showed in their Figure 6 (at $t/T=0.1$) that the maximum turbulent dissipation rate accounting for void fraction is about 3 times of that without considering void fraction. This is consistent with our observation at FOR station 1 (Figure 16a).

5.3. Turbulence Dissipation Rate Versus Total Energy Dissipation Rate

Following Lim *et al.* [2015], the total energy E (and therefore its dissipation)—considering the effects of void fraction—was computed as the sum of the period-averaged, depth-integrated mean kinetic energy K_{di} , the turbulent kinetic energy k_{di} , and the potential energy PE per unit mass as follows.

$$\begin{aligned}
 K_{di} &= \int_{-h}^{\eta} (1 - \langle \alpha \rangle) \frac{1}{2} (U^2 + W^2) dz \\
 k_{di} &= \int_{-h}^{\eta} (1 - \langle \alpha \rangle) \frac{1.33}{2} (\langle u'^2 \rangle + \langle w'^2 \rangle) dz \\
 PE &= \int_{-h}^{\eta} (1 - \langle \alpha \rangle) g z dz - \frac{1}{2} g h^2 \\
 E &= K_{di} + k_{di} + PE
 \end{aligned}
 \tag{16}$$

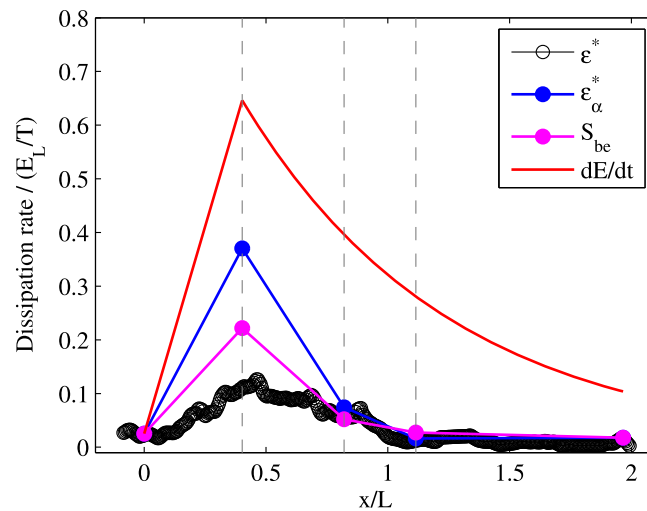


Figure 17. Normalized (by E_L/T) total energy dissipation rate dE/dt , turbulent dissipation rate with and without considering void fraction ε_α^* and ε^* , and bubble-induced energy dissipation rate S_{be} . The vertical-dashed lines indicate the locations of the three FOR stations.

energy dissipation rate dE/dt is calculated by differentiating equation (17) with respect to x and multiplying in the group velocity C_g as follows.

$$\frac{dE}{dt} = 1.72 \frac{C_g}{L} \exp(-1.17x/L) \quad \text{for } \frac{x}{L} > 0.33 \quad (18)$$

Equation (18) indicates that the maximum total energy dissipation rate occurs at $x/L \leq 0.33$. For $x/L \leq 0.33$, a linear increase of the dissipation from zero to dE/dt is assumed. This assumption of linear increment is based on the observation of the turbulence dissipation rate without considering the void fraction, as shown in Figure 17.

To investigate the ratio of the turbulence energy dissipation rate to the total energy dissipation rate, the depth-integrated, period-averaged turbulent energy dissipation rate with (ε_α^*) and without (ε^*) considering void fraction is computed as:

$$\varepsilon^* = \int_{-h}^{\eta} \overline{\varepsilon_w} dz \quad (19)$$

$$\varepsilon_\alpha^* = \int_{-h}^{\eta} \overline{\varepsilon_m} dz \quad (20)$$

Figure 17 shows the normalized total energy dissipation rate dE/dt versus ε^* and ε_α^* . As expected, in the figure the discrepancies between ε^* and ε_α^* are large—equivalent to 70%, 23%, and 23% of ε_α^* at the first, second, and third splash-ups, respectively. This indicates that the turbulent dissipation rate is significantly underestimated at the first splash-up roller region where the void fraction is high, while only moderately underestimated at the second and third splash-ups. On the other hand, the figure also shows a significant discrepancy between dE/dt and ε_α^* . The ratios of the turbulent dissipation rate to the total energy dissipation rate are about 57%, 19%, and 6% at FOR stations 1–3, indicating that a large portion of energy dissipation contributed to mechanisms other than the continuous phase turbulent dissipation. The average ratio of ε_α^* to the total dissipation rate, integrated from the breaking point to $x = 2L$, is only 33%. Similar observations were also reported by other researchers for surf zone breaking waves. Govender *et al.* [2004] reported that the dissipation rate due to turbulence is much lower (less than 1%) than the total energy dissipation rate estimated using the bore approximation. Huang *et al.* [2009] found that the turbulent dissipation rate at its maximum is only about 10% of the total energy dissipation rate. In these two studies, other mechanisms—such as the sloping-bottom shallow-water effects that involve energy reflection from the beach, energy transmission in the swash zone, and energy dissipation by bottom friction—may be responsible for the significant discrepancy in the energy dissipation rates. However, those effects do not exist in the

where η is the free surface elevation measured using images, and U and W are the mean horizontal and vertical velocities. The variation of total energy decreases relatively slowly before $x/L = 0.33$, then decreases rapidly beyond that point. This roughly follows the inverse trend with respect to the distance, as shown in Lim *et al.* [2015], and can be formulated as

$$\frac{E_x}{E_L} = 1.47 \exp(-1.17x/L) \quad (17)$$

for $\frac{x}{L} > 0.33$

where E_x is the breaking wave energy with void fraction considered, and E_L is the prebreaking wave energy. For $x/L \leq 0.33$, $E_x/E_L = 1.0$ is assumed due to the small energy variation and the lack of void fraction data. The total

present constant-depth deep-water case. The unaccounted for, or the excess, energy dissipation rate increased from 43% at the first splash-up roller to 81% and 94% at the second and third splash-ups—although the gap between the total energy dissipation rate and ϵ_2^* is more or less constant throughout the breaking process, as show in the figure. For energy conservation, such excess energy dissipation must be accounted for elsewhere. Such a discrepancy was not reported in single phase flows, making bubbles the primary cause.

5.4. Estimation of Bubble Energy Dissipation Rate

The present study uses void fraction and air-water mixture velocity to quantify the contribution of the liquid-phase turbulent dissipation, and its ratio, to the total energy dissipation under breaking waves with intense air entrainment. It is well known that bubbles induce significant turbulence modulation in aerated flows. The bubble effects on the turbulence energy budget are modeled through the additional source term S_{bk} in the $k-\epsilon$ equations [Troshko and Hassan, 2001; Ma et al., 2011] as follows.

$$S_{bk} = \frac{3}{4d} C_D \bar{\alpha} |v_r|^3 \quad (21)$$

where C_D is the drag coefficients, $\bar{\alpha}$ is the period-averaged void fraction, d is the mean bubble diameter, and v_r is the relative velocity between bubbles and water in the present study. For bubbles within the range of $r_p < r < 4$ mm—with r being the bubble radius, and r_p being the bubble radius above which the bubbles begin to oscillate as they rise through the bubble column ($r_p \approx 0.67$ mm at 20°C)—Leifer et al. [2000] developed the following approach to estimate v_r .

$$v_r = [v_{rm} + j_1(r - r_c)^{m_1}] \exp [j_2 T (r - r_c)^{m_2}] \quad (22)$$

where $v_{rm} = 222$ mm/s is the minimum velocity of an oscillating bubble, $r_c = 0.584$ mm is the critical radius below which bubbles do not oscillate, and T is the water temperature in Celsius. j and m are constants assigned the following values: $j_1 = 0.733$, $j_2 = 4.79 \times 10^{-4}$, $m_1 = -0.849$, and $m_2 = -0.815$. Accordingly, the relative velocities based on the bubble mean radii are 0.28, 0.29, and 0.34 m/s at FOR stations 1, 2, and 3, respectively. Troshko and Hassan [2001] further discussed that the bubble-induced production is related to the bubble-induced dissipation by the single empirical coefficient, $C_e = 0.45$, and it is universal for adiabatic bubbly flows. Following the relation, the depth-integrated bubble-induced dissipation rate can be estimated as

$$S_{be} = \int_{-h}^{\eta} S_{bk} C_e dz \quad (23)$$

The normalized bubble-induced dissipation rate, $S_{be}/(E_L/T)$, is plotted in Figure 17. The values are 0.24, 0.06, and 0.03 at FOR stations 1, 2, and 3, respectively. As shown in Figure 17, the contribution of S_{be} is significant at the first splash-up where a large volume of air is entrained. This value of 24% is significant, and accounts for about one-half of the excess energy dissipation of 47% at FOR station 1. At the subsequent second and the third splash-ups, the contributions of bubble-induced dissipation to the total energy dissipation are less significant. The low S_{be} (and low S_{bk}) is expected because of the low turbulent kinetic energy at these two FOR stations [Lim et al., 2015]. By integrating the dissipation rates from the breaking point at $x = 0$ to $x = 2L$, the total bubble-induced dissipation (S_{be}) is found as 23% of the total energy dissipation, while the excess energy dissipation is 67% (or total turbulent dissipation rate (ϵ_2^*) is 33%). Note that the energy dissipation rate contributed from the bubble break-up process is not considered in the current analysis; but it may be responsible (at least to a certain degree) for this discrepancy. Based on numerical simulations of plunging breaking waves, Derakhti and Kirby [2014] reported a 53% ratio of S_{be} to the total energy dissipation; which is about twice the 23% ratio estimated in the present study.

Martinez-Bazan et al. [1999] reported that the frequency of bubble break-up depends on the dissipation rate of fluid turbulent kinetic energy as well as the mother-bubble diameter. Their statistical model, developed based on experimental data, showed that the bubble break-up frequency increased as a power function of the turbulent dissipation rate, with the exponent being approximately constant and equal to 0.3. However, their model may not be directly applicable to the present study because they assumed very low void fraction ($\alpha < 10^{-5}$), and that the presence of air bubbles does not affect the evolution of turbulence. Although it is not our scope here, we believe that new wave breaking experiments—using different

surfactants to produce different numbers of bubbles (and thus different void fractions)—may be needed to prove the observations made here and to quantify the bubble break-up energy.

6. Conclusions

In this paper, we have presented quantitative measurements of turbulent flow fields and bubble-size distributions under deep-water plunging breaking waves using PIV, BIV, and FOR. The wavelet-based technique was applied to extract the vortical structures and estimate their length scales in the impinging and the splash-up rollers. Evolution of bubble sizes and numbers at the three splash-up rollers were investigated in conjunction with the swirling strength of the highly aerated flow fields. The turbulent dissipation rates were estimated based on mixture theory considering void fraction, and then compared with the total energy dissipation rates.

The vortical structures, and the corresponding length scales, were successfully extracted using the wavelet-based technique by identifying the local maximum intermittency measure. The distributions of L_{IMM} coincide well with classical measures of turbulence, such as swirling strength and vorticity. The estimated length scales of the vortical structures range from $0.05H$ to $0.15H$ during the initial impinging and the splash-up roller stages. The length scales estimated using the wavelet-based technique are comparable to the integral length determined from autocorrelation.

The distributions of number of bubbles, separated as small and large bubbles by an estimated Hinze scale of approximately 2 mm in chord length (or 3 mm in diameter), were correlated with the swirling strength. During the passage of the first impinging roller, the results show that the number of smaller bubbles ($s < 2$ mm) is well correlated with the swirling strength of the flow, but poor correlation was found for the larger bubbles. The results imply that the local swirling motion of the energetic eddies enhances the breakup of larger bubbles into smaller bubbles in the impinging roller. On the contrary, during the passage of the first splash-up roller the swirling strength does not show clear correlation with the number of bubbles generated. This indicates that the mechanism of shearing the larger bubbles off, and splitting them into smaller bubbles, is relatively infrequent in the splash-up roller.

The PDF of bubble size versus bubble number was presented to examine the power scaling and Hinze scale of bubbles. The results show that two distinct slopes were observed in the first impinging roller, the second impinging/splash-up roller, and the third impinging/splash-up roller. The Hinze scale and slopes of power-law scaling in these rollers compare well with previously reported values. On the contrary, in the first splash-up roller the power-law scaling for the larger bubble is flatter, implying that the bubble break-up events were not as frequent as those in the other rollers. The Hinze scale is also not evident in the first splash-up roller. The cause is not clear, but the very high void fraction in the roller is likely involved.

The turbulent dissipation rate was estimated based on the mixture viscosity model with and without considering void fraction. The results show that the turbulent dissipation rate is significantly underestimated if void fraction is not accounted for. The underestimation becomes greater for higher void fraction, reaching 70% in the initial impinging and the splash-up roller region. This implies that bubbles play a prominent role in enhancing the turbulent dissipation rate. With void fraction accounted for, the turbulent dissipation rate was found to be significantly lower than the rate of total energy dissipation. The ratio of the turbulent dissipation rate to the total energy dissipation rate is 57%, 19%, and 6% at FOR stations 1, 2, and 3, respectively, with an average ratio of 33% integrated from the breaking point to two wavelengths. This imbalance is consistent with observations previously reported on surf zone breakers. The 67% excess energy dissipation is likely caused by the presence of bubbles. The integrated bubble-induced dissipation is found to be 23%. Note that the bubble break-up process is not considered in the current analysis, but it may be responsible for the remaining imbalance.

Appendix A: Estimation of Turbulence Dissipation Rate

For a Newtonian fluid, the rate of dissipation of turbulent kinetic energy ε is defined as [Tennekes and Lumley, 1972]:

$$\varepsilon = 2\nu s_{ij}s_{ij} = \nu \left\langle \frac{\partial u'_i}{\partial x_j} \left(\frac{\partial u'_i}{\partial x_j} + \frac{\partial u'_j}{\partial x_i} \right) \right\rangle \quad (\text{A1})$$

where ν is the kinematic viscosity. The equation can be expanded and rewritten as:

$$\begin{aligned} \varepsilon = \nu & \left[2 \left\langle \left(\frac{\partial u'}{\partial x} \right)^2 \right\rangle + \left\langle \left(\frac{\partial u'}{\partial z} \right)^2 \right\rangle + \left\langle \left(\frac{\partial w'}{\partial x} \right)^2 \right\rangle + 2 \left\langle \left(\frac{\partial w'}{\partial z} \right)^2 \right\rangle + 2 \left\langle \frac{\partial u'}{\partial z} \frac{\partial w'}{\partial x} \right\rangle \right. \\ & + \left\langle \left(\frac{\partial u'}{\partial y} \right)^2 \right\rangle + \left\langle \left(\frac{\partial v'}{\partial x} \right)^2 \right\rangle + 2 \left\langle \left(\frac{\partial v'}{\partial y} \right)^2 \right\rangle + 2 \left\langle \frac{\partial u'}{\partial y} \frac{\partial v'}{\partial x} \right\rangle \\ & \left. + \left\langle \left(\frac{\partial v'}{\partial z} \right)^2 \right\rangle + \left\langle \left(\frac{\partial w'}{\partial y} \right)^2 \right\rangle + 2 \left\langle \frac{\partial v'}{\partial z} \frac{\partial w'}{\partial y} \right\rangle \right] \quad (\text{A2}) \end{aligned}$$

In order to estimate ε using the measured 2-D velocity field, the lateral velocity v and the gradient terms with respect to y were estimated based on various assumptions. *George and Hussein* [1991] proposed a locally axisymmetric turbulence approach, assuming that turbulence is invariant to rotations around an axis, and derived the turbulent energy dissipation rate ε_A as:

$$\varepsilon_A = \nu \left[- \left\langle \left(\frac{\partial u'}{\partial x} \right)^2 \right\rangle + 2 \left\langle \left(\frac{\partial u'}{\partial z} \right)^2 \right\rangle + 2 \left\langle \left(\frac{\partial w'}{\partial x} \right)^2 \right\rangle + 8 \left\langle \left(\frac{\partial w'}{\partial z} \right)^2 \right\rangle + 6 \left\langle \frac{\partial u'}{\partial z} \frac{\partial w'}{\partial x} \right\rangle \right] \quad (\text{A3})$$

Kimmoun and Branger [2007] assumed that $\langle (\partial u' / \partial y)^2 \rangle$, $\langle (\partial v' / \partial y)^2 \rangle$, $\langle (\partial v' / \partial x)(\partial v' / \partial z) \rangle$, and $\langle (\partial w' / \partial y)^2 \rangle$ can be neglected when compared with the other terms, and that $\langle (\partial v' / \partial x)^2 \rangle$ and $\langle (\partial v' / \partial z)^2 \rangle$ can be approximated as $[\langle (\partial u' / \partial x)^2 \rangle + \langle (\partial w' / \partial x)^2 \rangle] / 3$ and $[\langle (\partial u' / \partial z)^2 \rangle + \langle (\partial w' / \partial z)^2 \rangle] / 3$, respectively. Accordingly the turbulent energy dissipation rate, ε_C , is estimated as:

$$\varepsilon_C = \nu \left[\frac{7}{3} \left\langle \left(\frac{\partial u'}{\partial x} \right)^2 \right\rangle + \frac{4}{3} \left\langle \left(\frac{\partial u'}{\partial z} \right)^2 \right\rangle + \frac{4}{3} \left\langle \left(\frac{\partial w'}{\partial x} \right)^2 \right\rangle + \frac{7}{3} \left\langle \left(\frac{\partial w'}{\partial z} \right)^2 \right\rangle + 2 \left\langle \frac{\partial u'}{\partial z} \frac{\partial w'}{\partial x} \right\rangle \right] \quad (\text{A4})$$

Doron et al. [2001] proposed a "direct method" assuming that all lateral fluctuations have similar average magnitudes: the nonproduct terms $\langle (\partial u' / \partial y)^2 \rangle$, $\langle (\partial v' / \partial y)^2 \rangle$, $\langle (\partial v' / \partial x)^2 \rangle$, and $\langle (\partial v' / \partial z)^2 \rangle$ are approximated as $[\langle (\partial u' / \partial z)^2 \rangle + \langle (\partial w' / \partial x)^2 \rangle] / 2$; and the product terms $\langle (\partial u' / \partial y)(\partial v' / \partial x) \rangle$ and $\langle (\partial w' / \partial y)(\partial v' / \partial z) \rangle$ are approximated as $\langle (\partial u' / \partial z)(\partial w' / \partial x) \rangle$. Accordingly, the estimated turbulent energy dissipation rate ε_D becomes:

$$\varepsilon_D = \nu \left[3 \left\langle \left(\frac{\partial u'}{\partial x} \right)^2 \right\rangle + 3 \left\langle \left(\frac{\partial u'}{\partial z} \right)^2 \right\rangle + 3 \left\langle \left(\frac{\partial w'}{\partial x} \right)^2 \right\rangle + 3 \left\langle \left(\frac{\partial w'}{\partial z} \right)^2 \right\rangle + 6 \left\langle \frac{\partial u'}{\partial z} \frac{\partial w'}{\partial x} \right\rangle + 2 \left\langle \left(\frac{\partial u'}{\partial x} \frac{\partial w'}{\partial z} \right)^2 \right\rangle \right] \quad (\text{A5})$$

Cowen et al. [2003] applied a central difference technique to the product of fluctuating strain rate and used an empirical coefficient to estimate the turbulent energy dissipation rate ε_E as:

$$\varepsilon_E = 2\nu c_1 \left[\left\langle \left(\frac{\partial u'}{\partial x} \right)^2 \right\rangle + \frac{1}{2} \left\langle \left(\frac{\partial u'}{\partial z} \right)^2 \right\rangle + \frac{1}{2} \left\langle \left(\frac{\partial w'}{\partial x} \right)^2 \right\rangle + \left\langle \left(\frac{\partial w'}{\partial z} \right)^2 \right\rangle + \left\langle \frac{\partial u'}{\partial z} \frac{\partial w'}{\partial x} \right\rangle \right] \quad (\text{A6})$$

where the empirical coefficient $c_1 = 1.4$.

Acknowledgments

The authors wish to express thanks for the partial financial support provided by the Offshore Technology Research Center through its Industry Consortium under the projects entitled "Implementation of Bubble Image Velocimetry in OTRC Wave Basin," and for the partial support provided by the Haynes Coastal Engineering Laboratory. Z.C.H. was supported by the National Science Council in Taiwan under grant number MOST 104-2611-M-008-002. Data used in generating results in this study will be available upon request by contacting the corresponding author (KAC) at kchang@tamu.edu.

References

- Adrian, R. J., K. T. Christensen, and Z. C. Liu (2000), Analysis and interpretation of instantaneous turbulent velocity fields, *Exp. Fluids*, *29*, 2752-290.
- Baldy, S. (1988), Bubbles in the close vicinity of breaking waves, *J. Geophys. Res.*, *93*(C7), 8239-8249.
- Baldy, S. (1993), A generation-dispersion model of ambient and transient bubbles in the close vicinity of breaking waves, *J. Geophys. Res.*, *98*(C10), 18,277-18,293.
- Blenkinsopp, C. E., and J. R. Chaplin (2007), Void fraction measurements in breaking waves, *Proc. R. Soc. A*, *463*(2088), 3151-3170.
- Blenkinsopp, C. E., and J. R. Chaplin (2010), Bubble size measurements in breaking waves using optical fiber phase detection probes, *IEEE J. Oceanic Eng.*, *35*(2), 388-401.
- Bonnet, J. P., and J. Delville (2001), Review of coherent structures in turbulent free shear flows and their possible influence on computational methods, *Flow Turbul. Combust.*, *66*(4), 333-353.
- Camussi, R. (2002), Coherent structure identification from wavelet analysis of particle image velocimetry data, *Exp. Fluids*, *32*, 76-86.
- Camussi, R., and F. D. Felice (2006), Statistical properties of vortical structures with spanwise vorticity in zero pressure gradient turbulent boundary layers, *Phys. Fluids*, *18*, 035108.

- Chang, K. A., H. J. Lim, and C. B. Su (2002), A fibre optic Fresnel ratio meter for measurements of solute concentration and refractive index change in fluids, *Meas. Sci. Technol.*, *13*, 1962–1965.
- Chang, K. A., H. J. Lim, and C. B. Su (2003), Fiber optic reflectometer for velocity and fraction ratio measurements in multiphase flows, *Rev. Sci. Instrum.*, *74*(7), 3559–3565.
- Chanson, H. (2002), Air–water flow measurements with intrusive phase-detection probes: Can we improve their interpretation?, *J. Hydraul. Eng.*, *128*(3), 252–255.
- Clark, N. N., and R. Turton (1998), Chord length distributions related to bubble size distributions in multiphase flows, *Int. J. Multiphase Flow*, *14*(4), 413–424.
- Cowen, E. A., I. M. Sou, P. L.-F. Liu, and B. Raubenheimer (2003), PIV measurements within a laboratory generated swash zone, *J. Eng. Mech.*, *129*, 1119–2003.
- Cox, D. T., and N. Kobayashi (2000), Identification of intense, intermittent coherent motions under shoaling and breaking waves, *J. Geophys. Res.*, *105*(6), 223–236.
- Cox, D. T., and S. W. Shin (2003), Laboratory measurements of void fraction and turbulence in the bore region of surf zone waves, *J. Eng. Mech.*, *129*(10), 1197–1205.
- Deane, G. B. and Stokes, (2002), Scale dependence of bubble creation mechanisms in breaking waves, *Nature*, *418*, 839–844.
- Derakhti, M., and J. T. Kirby (2014), Bubble entrainment and liquid–bubble interaction under unsteady breaking waves, *J. Fluid Mech.*, *761*, 464–506.
- Doron, P., L. Bertuccioli, J. Katz., and T. R. Osborn (2001), Turbulence characteristics and dissipation estimates in the coastal ocean bottom boundary layer from PIV data, *J. Phys. Oceanogr.*, *31*, 2108–2134.
- Drazen, D. A., and W. K. Melville (2009), Turbulence and mixing in unsteady breaking surface waves, *J. Fluid Mech.*, *628*, 85–119.
- Farge, M. (1992), Wavelet transform and their applications to turbulence, *Annu. Rev. Fluid Mech.*, *24*, 395–457.
- Garrett, C., M. Li, and D. Farmer (2000), The connection between bubble size spectra and energy dissipation rates in the upper ocean, *J. Phys. Oceanogr.*, *30*, 2163–2171.
- George, W. K., and H. J. Hussein (1991), Locally axisymmetric turbulence, *J. Fluid Mech.*, *233*, 1–23.
- Govender, K., G. P. Mocke, and M. J. Alport (2004), Dissipation of isotropic turbulence and length-scale measurements through the wave roller in laboratory spilling waves, *J. Geophys. Res.*, *109*, C08018, doi:10.1029/2003JC002233.
- Hinze, J. O. (1955), Fundamentals of the hydrodynamic mechanism of splitting in dispersion processes, *AIChE J.*, *1*, 289–295.
- Huang, Z. C., S. C. Hsiao, H. H. Hwung, and K. A. Chang (2009), Turbulence and energy dissipations of surf-zone spilling breakers, *Coastal Eng.*, *56*, 733–746.
- Huang, Z. C., H. H. Hwung, and K. A. Chang (2010), Wavelet-based vortical structure detection and length scale estimate for laboratory spilling waves, *Coastal Eng.*, *57*(9), 795–811.
- Ishii, M. and K. Mishima (1984), Two-fluid model and hydrodynamic constitutive relations, *Nucl. Eng. Des.*, *82*, 107–126.
- Ishii, M. and N. Zuber (1979), Drag Coefficient and Relative Velocity in Bubbly, Droplet or Particulate Flows, *AIChE J.*, *25*, 843–855.
- Kiger, K. T., and J. H. Duncan (2012), Air-entrainment mechanisms in plunging jets and breaking waves, *Annu. Rev. Fluid Mech.*, *44*, 563–596.
- Kimmoun, O., and H. Branger (2007), A particle images velocimetry investigation on laboratory surf-zone breaking waves over a sloping beach, *J. Fluid Mech.*, *588*, 353–397.
- Lamarre, E., and W. K. Melville (1991), Air entrainment and dissipation in breaking waves, *Nature*, *351*, 469–472.
- Lamarre, E., and W. K. Melville (1992), Instrumentation for the measurement of void-fraction in breaking waves: Laboratory and field results, *IEEE J. Oceanic Eng.*, *17*(2), 204–215.
- Leifer, I., R. K. Patro, and P. Bowyer (2000), A study on the temperature variation of rise velocity for large clean bubbles, *J. Atmos. Oceanic Technol.*, *17*, 1392–1402.
- Lim, H. J., K. A. Chang, C. B. Su, and C. Y. Chen (2008), Bubble velocity, diameter, and void fraction measurements in a multiphase flow using fiber optic reflectometer, *Rev. Sci. Instrum.*, *79*, 125105.
- Lim, H. J., K. A. Chang, Z. C. Huang, and B. Na (2015), Experimental study on plunging breaking waves in deep water, *J. Geophys. Res. Oceans*, *120*, 2007–2049, doi:10.1002/2014JC010269.
- Lin, C., S. C. Hsieh, I. J. Lin, K. A. Chang, and R. V. Raikar (2012), Flow property and self-similarity in steady hydraulic jumps, *Exp. Fluids*, *53*, 1591–1616.
- Liu, W., and N. N. Clark (1995), Relationships between distributions of chordlengths and distributions of bubble sizes including their statistical parameters, *Int. J. Multiphase Flow*, *21*(6), 1073–1089.
- Liu, W., N. N. Clark, and A. I. Karamavruc (1996), General method for the transformation of chord-length data to a local bubble-size distribution, *AIChE J.*, *42*(10), 2713–2720.
- Longo, S. (2003), Turbulence under spilling breakers using discrete wavelets, *Exp. Fluids*, *34*, 181–191.
- Longo, S. (2009), Vorticity and intermittency within the pre-breaking region of spilling breakers, *Coastal Eng.*, *56*(3), 285–296.
- Ma, G. (2012), Multiscale numerical study of turbulent flow and bubble entrainment in the surf zone, PhD thesis, Univ. of Del., Newark.
- Ma, G., F. Shi, and J. T. Kirby (2011), A polydisperse two-fluid model for surf zone bubble simulation, *J. Geophys. Res.*, *116*, C05010, doi: 10.1029/2010JC006667.
- Manninen, M., V. Taivassalo, S. Kallio (1996), On the Mixture Model for Multiphase Flow, VIT Publications, *Technical Research Center of Finland*, *288*, 1–65.
- Martinez-Bazan, C., J. Rodriguez-Rodriguez, G. B. Deane, J. L. Montanes, and J. C. Lasheras (1999), On the breakup of an air bubble injected into a fully developed turbulent flow. Part 1. Breakup frequency, *J. Fluid Mech.*, *401*, 157–182.
- Melville, W. K., F. Veron, and C. J. White (2002), The velocity field under breaking waves: Coherent structures and turbulence, *J. Fluid Mech.*, *454*, 203–233.
- Mori, N., and S. Kakuno (2008), Aeration and bubble measurements of coastal breaking waves, *Fluid Dyn. Res.*, *40*, 616–626.
- Mori, N., T. Suzuki, and S. Kakuno (2007), Experimental study of air bubbles and turbulence characteristics in the surf zone, *J. Geophys. Res.*, *112*, C05014, doi:10.1029/2006JC003647.
- Nimmo Smith, W. A. M., J. Katz, and T. R. Osborn (2005), On the structure of turbulence in the bottom boundary layer of the coastal ocean, *J. Phys. Oceanogr.*, *35*, 72–93.
- Rapp, R. J., and W. K. Melville (1990), Laboratory measurements of deep-water breaking waves, *Philos. Trans. R. Soc. London A*, *331*, 735–800.
- Rensen, J., S. Luther, and D. Lohse (2005), The effect of bubbles on developed turbulence, *J. Fluid Mech.*, *538*, 153–187.
- Rojas, G., and M. R. Loewen (2007), Fiber-optic probe measurements of void fraction and bubble size distributions beneath breaking waves, *Exp. Fluids*, *43*, 895–906.

- Rojas, G., and M. R. Loewen (2010), Void fraction measurements beneath plunging and spilling breaking waves, *J. Geophys. Res.*, *115*, C08001, doi:10.1029/2009JC005614.
- Ruppert-Felsot, J., M. Farge, and P. Petitjeans (2009), Wavelet tools to study intermittency: Application to vortex bursting, *J. Fluid Mech.*, *636*, 427–453.
- Ryu, Y., and K. A. Chang (2008), Green water void fraction due to breaking wave impinging and overtopping, *Exp. Fluids*, *45*(5), 883–898.
- Ryu, Y., K. A. Chang, and H. J. Lim (2005), Use of bubble image velocimetry for measurement of plunging wave impinging on structure and associated greenwater, *Meas. Sci. Technol.*, *16*, 1945–1953.
- Saberi S., K. Shakourzadeh, D. Bastoul, and J. Militzer (1995), Bubble size and velocity measurements in gas liquid systems: Application of fiber-optic technique to pilot plant scale, *Can. J. Chem. Eng.*, *73*, 253–257.
- Serdula, C. D., and M. R. Loewen (1998), Experiments investigating the use of fiber-optic probes for measuring bubble-size distributions, *IEEE J. Oceanic Eng.*, *23*(4), 385–399.
- Serizawa, A., and I. Kataoka (1990), Turbulence suppression in bubbly two-phase flow, *Nucl. Eng. Des.*, *122*, 1–16.
- Shi, F., J. T. Kirby, and G. Ma (2010), Modeling quiescent phase transport of air bubbles induced by breaking waves, *Ocean Modell.*, *35*(1–2), 105–117.
- Skyner, D. (1996), A comparison of numerical predictions and experimental measurements of the internal kinematics of a deep-water plunging wave, *J. Fluid Mech.*, *315*, 51.
- Tennekes, L., and J. L. Lumley (1972), *A First Course in Turbulence*, Massachusetts Institute of Technology Press, Cambridge, Mass.
- Ting, F. C. K., and J. T. Kirby (1996), Dynamics of surf-zone turbulence in a spilling breaker, *Coastal Eng.*, *27*, 131–160.
- Troshko, A. A., and Y. A. Hassan (2001), A two-equation turbulence model of turbulent bubbly flows, *Int. J. Multiphase Flow*, *27*, 1965–2000.
- Vagle, S., and D. M. Farmer (1998), A comparison of four methods for bubble size and void fraction measurements, *IEEE J. Oceanic Eng.*, *23*(3), 211–222.
- Wang, S. K., S. J. Lee, O. C. Jones, and R. T. Lahey (1987), 3-D turbulence structure and phase distribution measurements in bubbly two-phase flows, *Int. J. Multiphase Flow*, *13*, 327–343.
- Watanabe, Y., H. Saeki, and R. J. Hosking (2005), Three-dimensional vortex structures under breaking waves, *J. Fluid Mech.*, *545*, 291–328.
- Zhou, J., R. J. Adrian, S. Balachandar, and T. M. Kendall (1999), Mechanisms for generating coherent packets of hairpin vortices in channel flow, *J. Fluid Mech.*, *387*, 353–396.